Bachelor Thesis

Contributions of massive stars and classical novae to Galactic ^{26}Al

Manja Zimmerer

Würzburg, September 19, 2025

Julius-Maximilians-Universität Würzburg
Lehrstuhl für Astronomie und Astrophysik
Betreuer: Dr. Thomas Siegert

Abstract

Context: The radioactive isotope ^{26}Al is thought to be mainly produced by massive stars. Its intermediate lifetime of 1.04 Myr is long enough that it is ejected into the interstellar medium, through winds or supernovae, before it decays. At the same time, this is short on Galactic timescales. ^{26}Al is therefore considered to trace the star formation rate (SFR) in the Galaxy. Recent measurements suggest a SFR $\gtrsim 5\,M_\odot\,\mathrm{yr}^{-1}$ [Siegert et al., 2023]. This exceeds other measurements by up to a factor of four [e.g., Kennicutt and Evans, 2012, Licquia and Newman, 2015, Chomiuk and Povich, 2011]. Other sources might also contribute to the Galactic budget of ^{26}Al, which would resolve this problem. A prime candidate are classical novae, as sites of explosive hydrogen burning, although previous studies show only negligible contributions or $\leq 10\%$.

Aims: The goal of this thesis is to determine the contribution of classical novae and massive stars to the Galactic budget of ^{26}Al.

Methods: First, different global models were tested in order to find a good starting point to assess the ^{26}Al mass as a function of Galactocentric radius. The Galaxy is then cut into concentric rings and different spatial models are tested in order to describe the distribution of the isotope throughout the Galaxy and fitted to 20 yr of INTEGRAL/SPI measurements. This yields the flux emissions at 1.8 MeV per distance, which is converted into the corresponding masses. Vasini et al. [2025] present a 2D Galactic Chemical Evolution (GCE) model, that yields the distribution of ^{26}Al throughout the Galaxy for novae and massive stars.

By assuming that the total mass is a linear combination of mass from these sources and adding scaling parameters, that describe the relative contribution, we can find the best parameter combination to fit these predictions via a χ^2 test. In order to account for other possible sources of ^{26}Al, we also consider very massive stars($\geq 120\,\mathrm{M}_\odot$ up to $500\,\mathrm{M}_\odot$), as modeled by Martinet et al. [2022] and test for combinations of those and classical novae.

Results: The amount of ^{26}Al found for a best fitting global model of the Galaxy is $M_{26} = 4.57 \pm 0.16\,\mathrm{M}_\odot$. We find that a doubly exponential disk with scale height $z_E = 0.6$ kpc and scale radius $R_E = 5.0$ kpc to be the best spatial model for the global Galaxy. For the dissected Galaxy, it is found that a doubly exponential disk with scale height $z_E = 0.4$ kpc and scale radius $R_E = 5.0$ kpc yields the best fits. This yields a total amount of $M_{26} =$

$2.24 \pm 0.61\,M_\odot$ within 15 kpc around the Galactic center. The local ^{26}Al distribution appears higher than predicted by GCE models. The contribution of novae is found to be non negligible with at least 62 %, when testing the GCE model from Vasini et al. [2025]. Contributions as shown in previous studies can only be found at the outer border of the 2σ confidence interval and appear rather unlikely. To explain the Galactic distribution of ^{26}Al throughout the Galaxy, massive stars alone are not sufficient. The results of this thesis show, that there must be a considerable amount of ^{26}Al that originated in classical novae or other sources that may be distributed similarly. All tested models, that are deemed likely, suggest, that it might even be the majority of Galactic ^{26}Al. This would relieve the tension in the SFR measurements, suggesting something more in line with other, independent measurements of the SFR.

Kurzfassung

Kontext: Es wird angenommen, dass das radioaktive Isotop ^{26}Al hauptsächlich von massereichen Sternen produziert wird. Seine mittlere Lebensdauer von 1,04 Myr ist lang genug, dass es durch die Winde oder Supernovae der Sterne in das interstellare Medium ausgestoßen wird, bevor es zerfällt. Gleichzeitig ist diese auf galaktischen Zeitskalen kurz. ^{26}Al wird daher als Indikator für die Sternentstehungsrate (SFR) in der Galaxie angesehen. Aktuelle Messungen deuten auf eine SFR $\gtrsim 5\,\mathrm{M_\odot yr^{-1}}$ hin [Siegert et al., 2023]. Das übersteig andere Messungen um bis zu einem Faktor vier [z.B., Kennicutt and Evans, 2012, Licquia and Newman, 2015, Chomiuk and Povich, 2011]. Andere Quellen könnten auch zum galaktischen Haushalt von ^{26}Al beitragen, was dieses Problem lösen könnte. Ein Hauptkandidat sind klassische Novae als Orte explosiven Wassterstoffbrennens, obwohl frühere Studien nur vernachlässibare Beiträge oder $\leq 10\,\%$ zeigen.

Ziele Das Ziel dieser Arbeit ist es die Beiträge von klassischen Novae und massereichen Sternen zum galaktischen ^{26}Al Haushalt zu bestimmen.

Methoden: Zunächst wurden verschiedene globale Modelle getestet, um einen guten Ausgangspunkt für die Bewertung der ^{26}Al Masse als Funktion des galaktozentrischen Radius zu finden. Anschließend wird die Galaxie in konzentrische Ringe unterteilt und verschiedene räumliche Modelle getestet, um die Verteilung des Isotops in der gesamten Galaxie zu beschreiben und an 20 Jahre Daten aus INTEGRAL/SPI Messungen anzupassen. Das ergibt die Flussemission bei 1.8 MeV pro Entfernung, die in die entsprechenden Massen umgerechnet werden. Vasini et al. [2025] stellen ein 2D-Modell der galaktisch chemischen Evolution (GCE) vor, das die Verteilung von ^{26}Al aus klassischen Novae und massereichen Sternen liefert. Unter der Annahme, dass die Gesamtmasse von ^{26}Al eine Linearkombination der beiden Quellen ist, und durch Hinzufügen von Skalierungsparameter, die den relativen Beitrag beschreiben, können wir die beste Parameterkombination finden, um diese Vorhersage mittels eines χ^2-Test anzupassen. Um auch andere mögliche Quellen für ^{26}Al zu berücksichtigen, betrachten wir auch sehr massereiche Sterne ($\geq 120\,\mathrm{M_\odot}$ up to $500\,\mathrm{M_\odot}$), wie sie von Martinet et al. [2022] modelliert werden, und testen Kombinationen aus diesen mit klassischen Novae.

Results: Die Gesamtmasse an ^{26}Al, die für ein am besten passendes globales Modell der Galaxie gefunden wurde, beträgt $M_{26} = 4.56 \pm 0.16\,\mathrm{M_\odot}$. Wir finden, dass eine doppelt

exponentielle Scheibe mit Skalenhöhe $z_E = 0.6\,\mathrm{kpc}$ und Skalenradius $R_E = 5.0\,\mathrm{kpc}$, das beste räumliche Modell für die globale Galaxie ist. Für die zerlegte Galaxie wurde festgestellt, dass eine doppelt exponentielle Scheibe mit einer Skalenhöhe von $z_E = 0.4\,\mathrm{kpc}$ und Skalenradius $R_E = 5.0\,\mathrm{kpc}$, die beste Übereinstimmung liefert. Diese ergibt eine Gesamtmasse von $M_{26} = 2.24 \pm 0.61\,\mathrm{M}_\odot$ innerhalb 15 kpc um das galaktische Zentrum. Die lokale ^{26}Al Verteilung scheint höher als von den GCE Modellen vorhergesagt
Der Beitrag von Novae zeigte sich als nicht vernachlässigbar mit mind. 62 % Anteil bei χ Minimum, für den Fit des GCE Models von Vasini et al. [2025]. Beiträge, wie sie in früheren Studien gezeigt wurden, finden sich nur am äußeren Rand des 2σ-Konfidenzintervalls und erscheinen eher unwahrscheinlich. Um die galaktische ^{26}Al Verteilung zu erklären, reichen massereiche Sterne nicht aus. Die Ergebnisse dieser Arbeit zeigen, dass eine beträchtliche Menge aus Novae oder anderen Quellen stammt, die ähnlich verteilt sein könnten. Alle getesteten Modelle, die als wahrscheinlich angesehen werden, legen nahe, dass es sich sogar um den Großteil des galaktischen ^{26}Al handeln könnte. Dies würde die Spannung in den SFR-Messungen verringern und deutet auf einen Wert hin, der eher mit anderen, unabhängigen Messungen der SFR übereinstimmt.

Contents

Chapter 1

Introduction

The radioactive isotope ^{26}Al has been studied for years, as it was the first cosmic radioactivity ever detected [Mahoney, 1984]. It is the source of the diffuse gamma-ray line emission at 1.8 MeV and thought to be mainly produced by massive stars. The all-sky map of the 1.8 MeV line, see Fig.1.1, shows extended emission along the entire Galactic plane, which corresponds to the distribution of massive-star groups. The overlay shows that a doubly exponential disk model traces the emission well, which motivates such a Galactic model, see Section 5.1.2.

Its intermediate lifetime of 1.04 Myr, allows for it to be long-lived enough, to be ejected into the interstellar medium (ISM), either during the wind phase or at the star's end

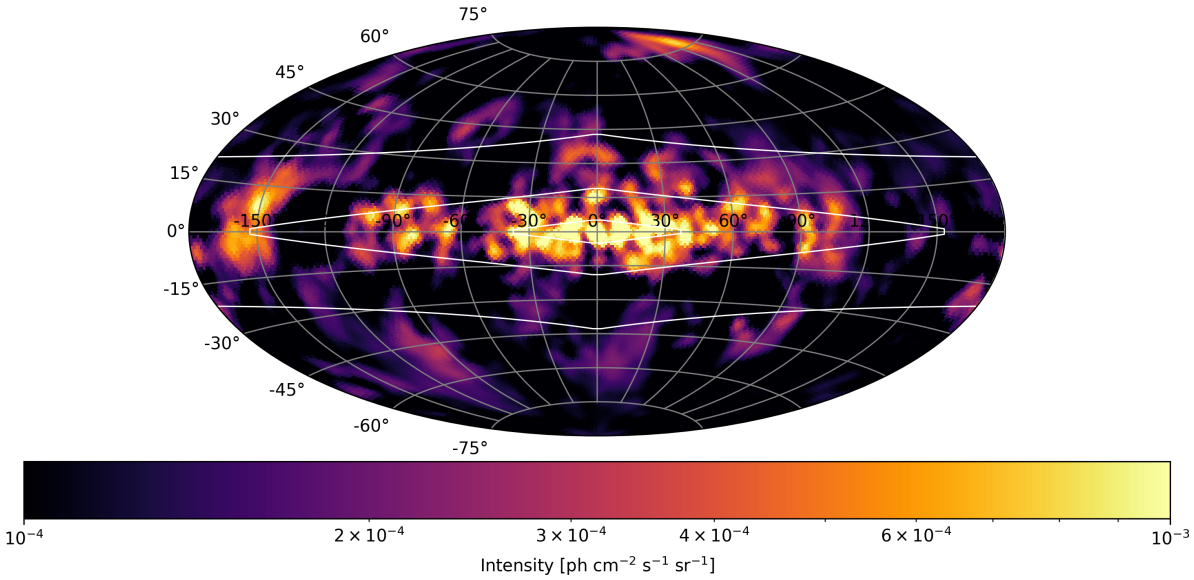

Figure 1.1: All-sky map of the Galactic ^{26}Al line at 1.8 MeV from Bouchet et al. [2015] overlaid by contours of an double exponential disk with scale radius $R_E = 5.0$ kpc and scale height $h_E = 0.6$ keV.

through a supernova. However, compared to the timescale of Galactic evolution, the lifetime is short. We therefore only detect the ^{26}Al produced within the last 50 Myr and consider it to be an excellent tracer of the ongoing nucleosynthesis in our Galaxy. ^{26}Al measurements can be used to calculate the Galactic star formation rate (SFR). This results in SFR $\gtrsim 5\ \mathrm{M_\odot\,yr^{-1}}$ [Siegert et al., 2023]. However, other methods only suggest a SFR of 1–2 $\mathrm{M_\odot yr^{-1}}$.[e.g., Kennicutt and Evans, 2012, Licquia and Newman, 2015, Chomiuk and Povich, 2011]. If all ^{26}Al only originated in massive star nucleosynthesis, we would be short of up to four times the mass that should be produced in our Galaxy. This excess of ^{26}Al could be explained if another source is found to produce considerable amounts of the isotope.

In principle, all environments of hydrogen burning are potential sources of ^{26}Al. While all main sequence stars experience hydrogen burning, massive stars, i.e. stars with an initial mass larger than 8 $\mathrm{M_\odot}$, evolve quickly throughout the main sequence. They still contain a considerable amount of ^{26}Al when entering the wind phase, that can then be distributed into the ISM. Stars of this mass are typically thought to end in core-collapse supernovae. In the explosion, that is if they explode at all, they contribute even more ^{26}Al to the Galactic budget.

Another site of explosive hydrogen burning are classical novae. These are hosted in binary systems, consisting of a white dwarf and a, typically main sequence, companion. The white dwarf accretes matter through the Roche lobe of the system. The matter closest to the surface of the white dwarf gets compressed to the point of degeneracy. This leads to a decoupling of pressure and heat in the accreted envelope. In a thermonuclear runaway, fusion processes are ignited, further heating the system. At some point, the system becomes hot enough to cross the degeneracy line again, which leads to a rapid expansion of the matter and the ejection of the outer layers. During these fusion processes, ^{26}Al could be fused in considerable amounts, making classical novae a prime suspect of a source José [2016].

The goal of this work is to determine the contribution of classical novae and massive stars to the Galactic 1.8 MeV line measured with INTEGRAL/SPI over the course of 20 yr. Different models of the Galaxy were probed and compared to the GCE Model of Vasini et al. [2025] and the Evolution Model of Martinet et al. [2022] in order to assess the mass of ^{26}Al as a function of Galactocentric radius. This thesis is structured as follows: Chapter 2 gives an overview of the production sites and mechanisms of Galactic ^{26}Al as well as a short summary of the state of the art Galactic models of Vasini et al. [2025] and Martinet et al. [2022]. Thereafter, Chapter 3 gives a synopsis of the COMPTEL and INTEGRAL mission and the function of SPI. In Chapter 4 the data analysis method is presented, and statistical methods are discussed. The astrophysical modeling is explained in Chapter 5. Then, in Chapter 6, the results considering the gamma-ray line itself as well as flux and

mass values are presented for different Galactic models. This also includes χ^2 test results yielding the relative contributions of the considered sources. Finally, a summary is given in Chapter 7.

Chapter 2

^{26}Al — Theory and Predictions

2.1 Galactic ^{26}Al

The rather long lifetime of ^{26}Al ($\tau = 1.4$My), compared to similarly light nuclei, provides a special opportunity for tracing stellar nucleosynthesis as it has a chance to decay only after being ejected into the ISM [Diehl et al., 2020]. At the same time it's short-lived enough to be a demonstration that nucleosynthesis is an ongoing process in our Galaxy as it's lifetime is still much shorter than the time scale of galactic evolution ($\approx 10^{10}$yr) [Prantzos and Diehl, 1996].
This long lifetime is caused by the unusually high 5+ spin ground state. Compared to the ^{26}Mg isotope with 2+ and 0+, the difference in angular momentum is rather large. Excited ^{26}Al states have lower differences in angular momentum to ^{26}Mg and therefore shorter lifetimes. High enough temperatures could lead to thermally excited metastable states which decay without gamma-ray emission [Diehl et al., 2020]. The ground state of ^{26}Al decays mostly through the β^+-channel into an excited state of ^{26}Mg.

$$^{26}_{13}\mathrm{Al} \longrightarrow {}^{26}_{12}\mathrm{Mg}^{\,*} + \mathrm{e}^+ + \nu_e \tag{2.1}$$

$$^{26}_{12}\mathrm{Mg}^{*} \longrightarrow \gamma(1.8\mathrm{MeV}) + {}^{26}_{12}\mathrm{Mg} \tag{2.2}$$

In this process, a proton is converted into a neutron and together with a positron, an electron neutrino is emitted. This reduces the charge of the nucleus by 1. The excited ^{26}Mg relaxes to the ground state by emitting gamma-ray at 1.809MeV. This is the signature line for the identification of ^{26}Al [Diehl et al., 2020, 1994]. The decay scheme is shown in Fig.2.1.

^{26}Al is mainly produced by ^{25}Mg capturing a proton, i.e. $^{25}\mathrm{Mg}(\mathrm{p},\gamma)\,^{26}\mathrm{Al}$. Therefore, considerable amounts of ^{26}Al must be formed in ^{25}Mg- or proton-rich environments [Prantzos and Diehl, 1996]. These are encountered in different processes and will be discussed in the following chapters.

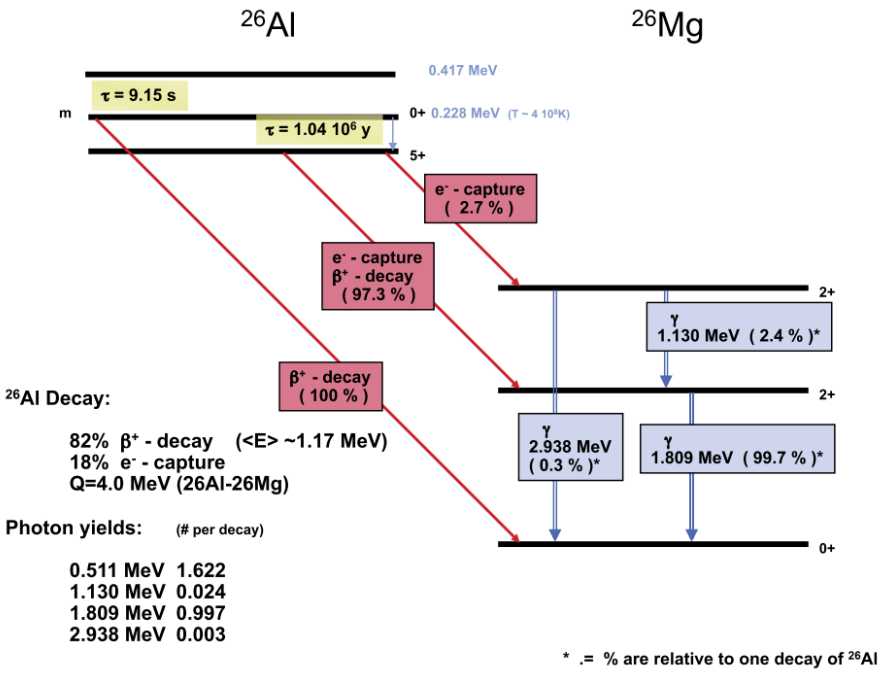

Figure 2.1: Schema of the radioactive decay of ^{26}Al. Due to the large spin difference to the daughter nucleus, the ground state of ^{26}Al has a rather long lifetime of $1.04\,\mathrm{My}$. It decays into an excited state of ^{25}Mg with a lifetime of $\tau = 687\,\mathrm{fs}$ [National Nuclear Data Center (NNDC)]. The gamma-ray line of $1.809\,\mathrm{MeV}$ is used to track ^{26}Al throughout the Galaxy [Diehl, 2021]

.

2.2 Stellar Evolution

Stars are born out of contracting interstellar clouds. If the gravitational energy is stronger than the thermal energy, the particles are pulled together and with increasing density the temperature rises. This is called a *protostar*. When, eventually, pressure and temperature at the center of the protostar become high enough, core burning sets in. This marks the transition from the Hayashi track to the main sequence on the Hertzsprung-Russel diagram, making it a *zero age main sequence star*(ZAMS). The inner core is now in hydrostatic equilibrium as the radiation pressure prevents a gravitational collapse and the star will spend about 80% of its lifetime here as an *main sequence star*. In its life, it will evolve along the main sequence as *hydrogen burning* goes on [Hanslmeier, 2020, p 442 et sqq].

Depending on the temperature, different burning cycles dominate the core burning. For temperatures between 5 and 15 MK hydrogen burns into helium via the proton-proton chain (p-p chain). There are minor differences between the three possible pp cycles but as the *proton-proton-I-chain* (ppI) is the dominant one, it is the one being shown here

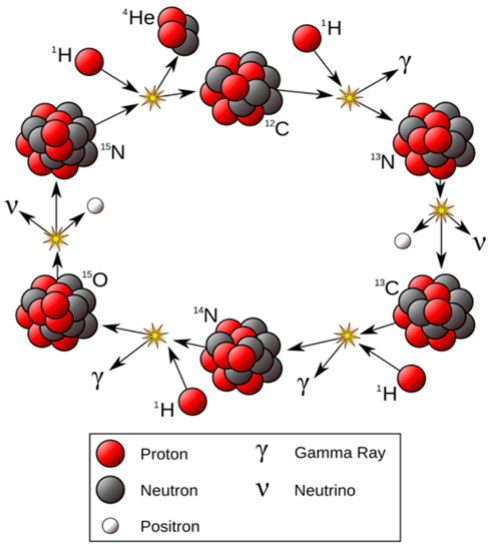

Figure 2.2: In more massive stars, hydrogen mostly burns through the shown Carbon-Nitrogen-Oxygen-cycle (CNO). Carbon is only used as catalysts and therefore does not get wasted throughout the process.[1]

[Hanslmeier, 2020, p.410]:

$$^1\mathrm{H} + {}^1\mathrm{H} \longrightarrow {}^2\mathrm{H} + \mathrm{e}^+ + \nu \tag{2.3}$$

$$^2\mathrm{H} + {}^1\mathrm{H} \longrightarrow {}^3\mathrm{He} + \gamma \tag{2.4}$$

$$^3\mathrm{He} + {}^3\mathrm{He} \longrightarrow {}^4\mathrm{He} + 2\,{}^1\mathrm{H} \tag{2.5}$$

For higher temperatures, hydrogen burns in the *carbon-nitrogen-oxygen-cycle* (CNO-cycle). It requires the presence of heavier elements as catalysts and has the same outcome as the pp chain. A schematic overview is given in Figure 2.2. Similarly to the pp-chains, there are CNO-subbranches that differ slightly. For example, in the CNO II, the ^{15}N does not produce ^{12}C but the reaction proceeds though $^{15}\mathrm{N}(\mathrm{p},\gamma)^{16}\mathrm{O}(\mathrm{p},\gamma)^{17}\mathrm{F}(\beta^+)^{17}\mathrm{O}(\mathrm{p},\alpha)^{14}\mathrm{N}(\mathrm{p},\gamma)^{15}\mathrm{O}$.

The high temperature requirements and the need for carbon are the reason why the CNO-cycle is more dominant in more massive stars ($M_* > 1.2M_\odot$) [Heyssler, 2015, p.33].

The next and final stage of stellar evolution starts, when most hydrogen has been burned. At its current state, the star has a core mostly consisting of helium surrounded by an envelope of still burning hydrogen. The thermonuclear reaction in the core first ceases as the temperature is not high enough yet to start further burning processes. This also means there is no radiative pressure working against the gravitational pressure anymore, leading to an increase in pressure and consequently in heat. Only when the core temperature reaches 10^8K, helium begins to fuse in the so-called *triple-alpha process* [Hanslmeier,

2020]. Two ^{4}He are fused to an instable ^{8}Be-nucleus with a lifetime of 0.1 seconds. Only if another helium-nucleus is available to react with, stable ^{12}C is achieved. This will then be converted into ^{16}O [Hanslmeier, 2020, p.412]:

$$^4\mathrm{He} + {}^4\mathrm{He} \longleftrightarrow {}^8\mathrm{Be} \tag{2.6}$$

$$^8\mathrm{Be} + {}^4\mathrm{He} \longrightarrow {}^{12}\mathrm{C} + \gamma \tag{2.7}$$

$$^{12}\mathrm{C} + {}^4\mathrm{He} \longrightarrow {}^{16}\mathrm{O} + \gamma \tag{2.8}$$

Just as after hydrogen burning, a thin shell of burning helium remains around the new CO-core. The further evolution of the star now depends completely on its initial mass. Stars of lower and middle mass ($M_* \leq 8\mathrm{M}_\odot$) experience a so called Helium-flash, a sudden explosion allowing its core to expand. This leads to a decrease of the triple-alpha process and the start of carbon burning. If the carbon reserves are spent, the star collapses into a white dwarf, rejecting the outer hydrogen- and helium shells. A planetary nebula is left [Heyssler, 2016, p. 22].
For more massive stars, $M_* > 8\mathrm{M}_\odot$, the new core shrinks, causing the temperature to increase, and higher burning stages set in, if their threshold temperature is reached. For temperatures around $1.5 \times 10^8 - 10^9\,\mathrm{K}$ carbon burning sets in. This results, among other elements, in various magnesium isotopes, which are later important for the nucleosynthesis of aluminum-isotopes.
Then, for even higher temperatures, starting at $1.4 \times 10^9\,\mathrm{K}$ oxygen starts to burn into silicon and phosphorus. The silicon will finally start burning starting at $T \approx 2 \times 10^9\,\mathrm{K}$ in many different reactions, the most important being the one leading to stable ^{56}Fe, marking the end of fusion, as iron has the highest binding energy per nucleon. Further reactions would not lead to a release but a drain of energy. The end of fusion leads to the collapse of the star under its own weight as the equilibrium of radiative and gravitational forces breaks down. The resulting shockwave accelerates mostly all the stars mass outward while the inner part is still compressing, finally leaving behind either a black hole or a neutron star. This is called a core-collapse Supernova [Heyssler, 2016, p. 23]

2.3 Core-collapse Supernovae

A supernova is the explosion of a star, which ejects the outer envelope completely. They occur at a rate of $R_{\mathrm{SNe}} = 0.02\,\mathrm{yr}^{-1}$, [Siegert et al., 2023] in our Galaxy and are important sources of different isotopes.
Supernovae are classified into different types, defined by their progenitors but also by their spectroscopic features [Hanslmeier, 2020, José, 2016]. The absence of hydrogen lines distinguishes the difference between type I an II supernovae. type II, or core-collapse, supernovae show a widespread dispersion in absolute magnitudes and are in general dimmer

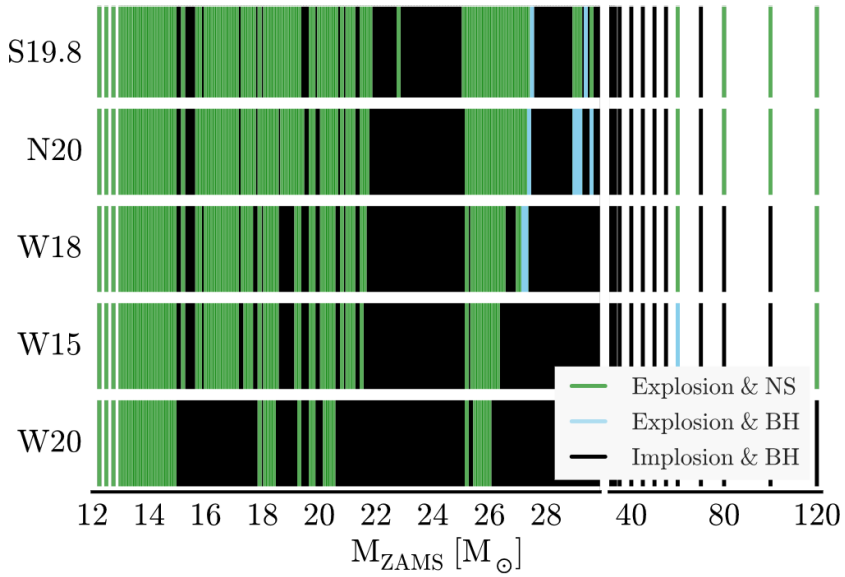

Figure 2.3: Explosion outcomes of five different models for a supernova explosion for different ZAMS masses up from 12.5 $M_\odot$. Models marked in black imploded and became a black hole. In green and blue are successful explosions leaving behind either a neutron star or a black hole, respectively [Sukhbold et al., 2016].

than type I. The profile of the light curve yields a lot of information about the exploding star, i.e. size, mass and composition, but also about the underlying neutron star and and the synthesis of radioactive isotopes.

Massive stars are thought to end in core-collapse supernovae, caused by the end of fusion processes. The radiative forces break down, and the core shrinks under its own weight. This causes the density to increase drastically. The pressure degenerates under these conditions, as the electrons have to obey Pauli's exclusion principle and are therefore forced to occupy different energy levels, if packed closely enough. This supports the core for a while, but the silicon burning shell is still supplying core mass. At some point the core exceeds the Chandrasekhar($M_{\mathrm{Ch}} \sim 5.76\, Y_e^2 \mathrm{M}_\odot$, where $Y_e = Z/A$ denotes the electron fraction) mass and becomes gravitationally unstable. This leads to the collapse of the star.

The transition mechanisms from implosion to explosion is debated. The shock wave caused by the incompressibility of the core, when modeled, shows to be too weak to transport the matter outwards. Another model suggests that neutrinos might carry the energy needed to ignite the explosion [Heyssler, 2016, José, 2016]. However, detailed simulations revealed, that more neutrinos than anticipated were trapped inside the core. One simulation, leading to a successful explosion, found that shortly, several hundred milliseconds, after the shock a weak explosion developed. This was caused by diffuse neutrino heating from the newly formed neutron star [José, 2016].

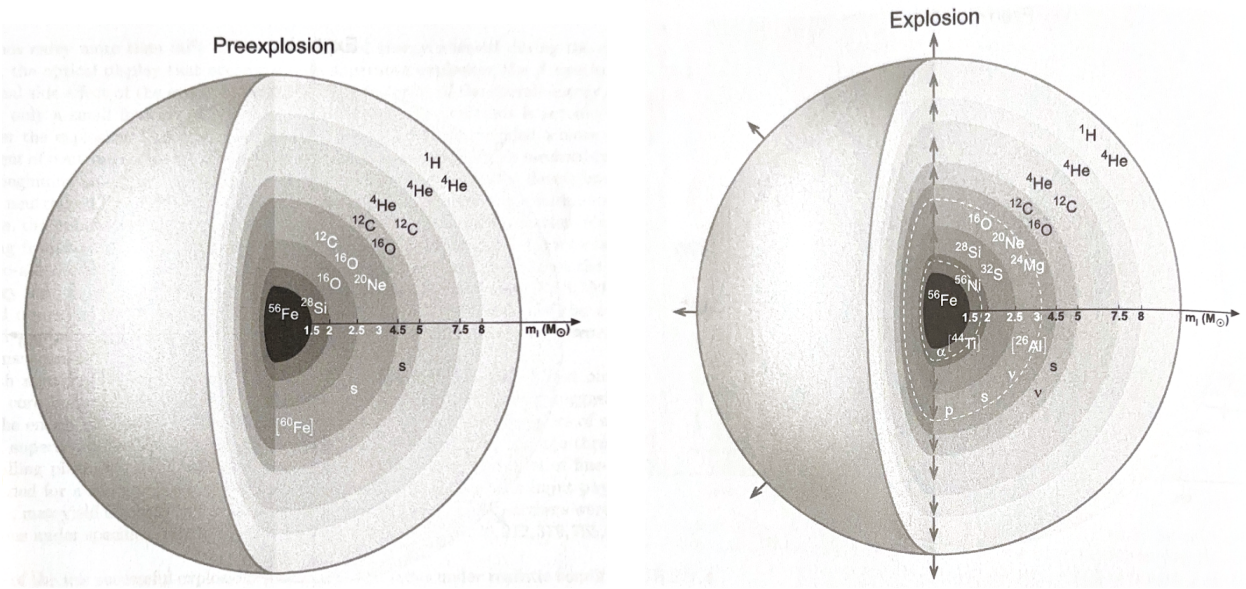

Figure 2.4: Structure of a massive star shortly before and during explosion. The onion like structure is a result of the successive nuclear burning stages during the stellar evolution. The shock wave during the explosion induces further nuclear burning in these shells [José, 2016].

Sukhbold et al. [2016], present the explosion outcome for stars of masses between $8 - -120\,\mathrm{M}_\odot$ for different simulations. They find that many stars do not explode at all, but implode and become black holes directly. Those stars would only contribute through their winds to the Galactic amount of ^{26}Al. The output of five simulations, depending on the ZAMS mass of the star is shown in Fig. 2.3.

The shock wave induces further nuclear activity. This will be sketched for a $25\,\mathrm{M}_\odot$ supernova progenitor of solar composition. Its shell structure before the explosion is shown on the left hand side in Fig. 2.4. The layers are encountered by the shock in an outwards direction. The first layer that is encountered is dominated by ^{28}Si and explosive silicon burning is ignited. This causes temperatures of $T \geq 5\,\mathrm{GK}$. The ash is made from ^{56}Ni with traces of ^{57}Ni,^{55}Co, and ^{54}Fe. The shell expands and cools down. At temperatures of $T \sim 4 - 5\,\mathrm{GK}$, the nuclear reactions break down in two quasi equilibrial regimes. One is forming around ^{28}Si, extending up to nuclei with $A \sim 40$. The other includes species with $A \geq 50$ and is centered around the Fe-peak nuclei. The specific composition is depending on the amount of available neutrons, the temperature, the abundance of ^{28}Si and the density. As a considerable amount of ^{28}Si is left, this is called *incomplete silicon burning*. Propagating outwards, the shock now reaches a layer rich in ^{16}O and causes explosive oxygen burning at temperatures around $T \sim 3 - 4\,\mathrm{GK}$. After the reactions freeze out, ^{28}Si, ^{32}S, ^{36}Ar and ^{40}Ca are the most abundant species. The final stage of explosive burning is encountered now. A layer, rich in ^{16}O, ^{12}C and ^{20}Ne, gets heated to

$T \sim 2 - 3\,\mathrm{GK}$ by the shock wave and ^{20}Ne and ^{12}C explosive burning begins. Due to the low temperatures, this happens far from any equilibrium, and the abundances expected after burning ceases are mostly depending on the initial composition and less on temperature and density. The resulting nuclei after freeze out are ^{16}O, ^{20}Ne, ^{24}Mg, ^{28}Si and ^{26}Al. The layers even further out are not heated enough to experience major burning anymore [José, 2016]. The estimated steady-state production rate of ^{26}Al is $2.0 \pm 1.0\,\mathrm{M_\odot yr^{-1}}$ for core-collapse supernovae [Timmes et al., 1995].

2.4 Classical Novae

This event originally got its name because of its sudden appearance. A very bright 'new star' (or in Latin *stella nova*) emerged in the sky. This bright signal, however, is only a transient event and will fade again in the following months. In reality, this phenomenon is the observation of a stellar explosion in a close binary system, consisting of a white dwarf (WD) accreting matter from its companion star. These systems are so called *cataclysmic variables* and can be subject to various types of outbursts, the second, most common type being novae eruptions (the first being X-ray bursts) [José et al., 2006]. The exchange of matter between these stars happens, because the companion, most commonly a star close to the main sequence, overflows its Roche lobe, which is the area around each of the stars in the binary system, in which matter is gravitationally bound. They are tear-shaped and connected in the inner Lagrangian point. Hydrogen rich matter flows through this point and, because of its angular momentum, forms an accretion disk around the WD. The fraction of matter directly on top of the WD is gradually compressed, due to the continuous infall of material and becomes more and more dense. Caused by the high density, the accreted matter becomes degenerate. At this point, the overall pressure is not coupled with the temperature anymore, meaning that a degenerate stellar plasma cannot simply increase its volume to self regulate if its heated [José, 2016]. The degenerate matter in the binary system is heated by compression and the WD itself. As it cannot expand, this leads to a thermonuclear runaway (TNR), which describes a self-accelerating process, i.e. one that is accelerated by hot conditions and at the same time releasing heat into its system. [José et al., 2006]. Fusion processes are ignited in the heated gas atmosphere, which as discussed before are exothermal and therefore releasing even more heat into the system. During this, critical, short-lived β-unstable isotopes are produced, the most important being ^{15}O, which is part of the CNO-cycle. The isotopes themselves, decay in the next few minutes, which again releases energy into the gas. This is a way more effective heating process than the radiative and conductive processes, and heats the atmosphere quickly. As soon as the temperature rises above the degeneracy line, the gas can suddenly self regulate again, and the layer above the nuclear reaction is expelled

[Shore, 2012]. The ejection is accompanied by an large increase of luminosity, with peak luminosities reaching $10^5\,L_\odot$ [José, 2016]. This was the bright signal originally observed.

The explosion does not disrupt the WD itself, as it would in a type Ia supernovae, but is restricted to the outer envelope. The star remains and resumes to accrete mass from its companion. All novae are therefore supposedly recurring events. Classical novae are expected to recur with a periodicity of the order of $10^4 - 10^5$ years, however 10-100 years have been observed. [José et al., 2006]. The predicted nova rate in the Milky Way is with $R_{\mathrm{CN}} = 50^{+31}_{-23}\,\mathrm{yr}^{-1}$ much higher than the rate of supernovae [Shafter, 2017]. The total ejected mass, however, is much smaller ($10^{-3} - 10^{-7} M_\odot$) than the mass ejected in a supernova and shows slower mean ejection velocities (on the order of several $10^3\,\mathrm{km\,s}^{-1}$) [José, 2016, p 151].

As discussed in Section 2.2, stars of low- and intermediate mass are the progenitors of white dwarfs.

Those with masses smaller than $\sim$ 7-8 $M_\odot$ experience hydrogen and helium-burning and evolve into a white dwarf rich in carbon and oxygen. These CO white dwarfs are the most frequent case. For progenitors with up to $\sim 10\,M_\odot$ carbon burning sets in but the conditions needed for neon burning are not reached. This leads to a white dwarf rich in oxygen and neon, with traces of magnesium and sodium, we call these ONe white dwarfs. The composition of the white dwarf in the binary system is relevant as convection processes mix some of the core matter with the accreted envelope. These are enriching it in seed nuclei, which are later responsible for specific reaction chains during the TNR [José et al., 2006, Casanova et al., 2018, e.g].

For CO novae the CNO-cycle dominates the fusion processes, mainly through the $^{12}\mathrm{C}(\mathrm{p},\gamma)\,^{13}\mathrm{N}(\beta^+)^{14}\mathrm{N}$ chain because of the higher ^{12}C concentration. The fusion process shows only minor activity for intermediate-mass elements [José and Hernanz, 1998, José, 2016]. For ONe novae the CNO cycle is, due to a lack of carbon, much less important. The NeNa-MgAl region however is very active, due to the pre-existing neon [José, 2016]. Only ONe novae are therefore a prime candidate to synthesize ^{26}Al and this thesis is going to focus on them. Novae showing bright neon lines are often called *neon* novae.

An illustrative overview of the nucleosynthesis products for different temperatures can be given if certain initial conditions are assumed. José [2016, p 161 et sqq], e.g., assume an initial mass of $1.15\,M_\odot$, initial luminosity of $10^{-2}\,L_\odot$ and a constant rate of mass accretion of $1.6 \times 10^{-10}\,M_\odot\,\mathrm{yr}^{-1}$ and evolve both models, ONe and CNO progenitors, with the 1D hydrodynamics code SHIVA. For the onset of accretion temperatures at the envelope base are well below $10^7\,\mathrm{K}$. At that time, fusion reactions are dominated by the pp-chains. This is true for both ONe- and CO- novae, even though the second already show minor contributions of the CNO cycle. For $T = 1.1 \times 10^7\,\mathrm{K}$ the CNO cycle already dominates fusion processes and more energy is released in the CO model than in the

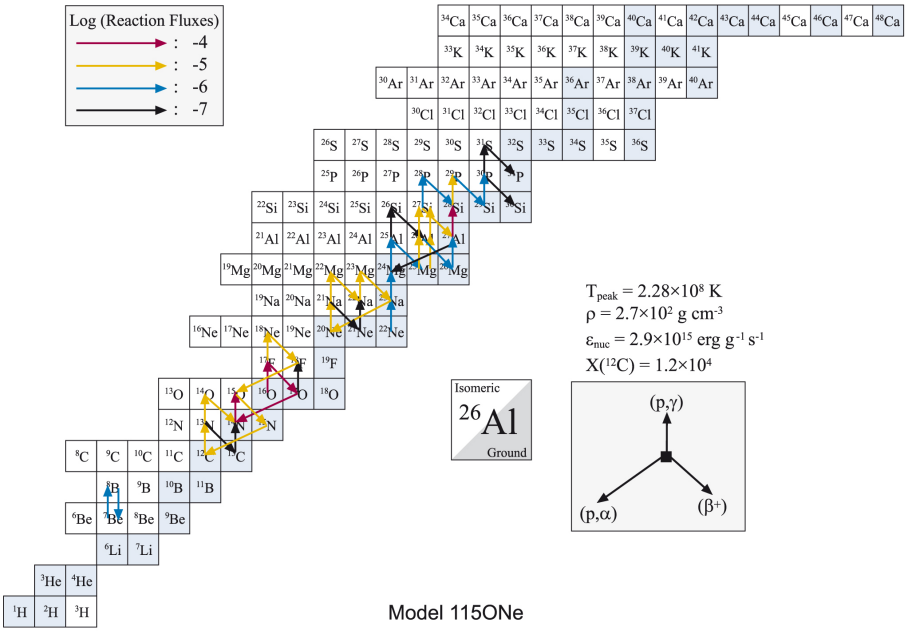

Figure 2.5: Nucleosynthesis processes during the envelope burning of a ONe novae with initial mass of 1.15 $M_\odot$ at peak temperature. The most relevant reactions are shown in terms of *reaction fluxes*, giving the number of reactions per unit time. The isotopes highlighted in blue are stable. [José, 2016]

ONe Model. For this reason the ONe model can accrete a lot more matter, before the degeneracy line is crossed. This also affects the densities and pressure in the envelope, which is directly responsible for the strength of the outburst. For both models the main nuclear path is always close to the valley of stability at peak temperature and driven by proton capture and β^+- decays. The main reaction fluxes for the inner envelope shell at peak temperatures for an ONe novae are shown in Fig. 2.5. It shows high CNO activity, especially the CNO II chain, $^{16}\mathrm{O}(\mathrm{p},\gamma)\,^{17}\mathrm{F}(\beta^+)\,^{17}\mathrm{O}\,(\mathrm{p},\alpha)\,^{14}\mathrm{N}(\mathrm{p},\gamma)\,^{15}\mathrm{O}$, and the $^{27}\mathrm{Al}(\mathrm{p},\gamma)^{28}\mathrm{Si}$ chain are dominating the nuclear reactions. The nuclear reactions for ONe envelopes extend up to ^{31}Si, which is, even though the peak temperature is somewhat higher, a consequence of the presence of ^{20}Ne as seed nuclei [José, 2016].

2.5 Galactic Chemical Evolution Models

Galactic Chemical Evolution (GCE) investigates the transformation of gas into stars and the resulting evolution of the chemical composition of a galaxy [Prantzos, 2008]. It allows to check our understanding of nucleosynthesis in a statistical way by comparing GCE model yields for stars of different masses (and metallicities, which describe the abundance of elements heavier than He in an object) with measurements of our Galaxy. It helps to give events a chronological order and delivers information of how a system was formed by

tracking specific markers, i.e. abundances of a specific nuclide or constraining different mechanisms.

An GCE model would consist of a primordial gas composition of mostly hydrogen, an adequate amount of helium plus some trace amounts of slightly heavier elements. This is turned into stars using a SFR$\Psi(t)$. The mass of the star M is following the distribution called *Initial Mass Function*(IMF). This may in principle be time dependent either directly or implicitly by a dependence on the metallicity. During its lifetime τ_M nuclear reactions are enhancing the metallicity of the star, and part of the mass is re-ejected into the ISM either through stellar winds or through a supernova explosion. The composition of the ISM therefore changes and the new stellar generation does show progressively higher metallicity [Prantzos, 2008].

Such a toy model is not taking into account the change of the ISM depending on the distance to the Galactic center, the supernova outburst rate in the Galaxy or the Spiral arm pattern of the Milky Way.

2.5.1 Tracing ^{26}Al in the spiral arms of the Milky Way

Vasini et al. [2025] published their results of a two-dimensional GCE model of our Galaxy, with the aim to predict the ^{26}Al mass as a function of Galactocentric radius. They account for the spiral pattern of the Milky Way by considering an spiral perturbation and use the SFR and the nova rate as inputs for their model. They considered a nova population consisting of 70 % CO novae and 30 % ONe novae and modeled the yields accordingly to José and Hernanz [2007]. As this depends on the initial mass, they chose the average of those used in José and Hernanz [2007], based on Romano and Matteucci [2003]. The yield of massive stars were the ones presented in Kobayashi et al. [2006] combined with the results for ^{26}Al from Woosley and Weaver [1995]. While these models are relatively old, a good order of magnitude estimate can be provided. A more recent model is described in Martinet et al. [2022]. The disk SFR peakes around 2.25 Gyr after the begin of the Milky Way evolution, around 1 Gyr before the perturbation of the SFR kicks in. At that time, the spiral arm pattern is easily recognized by tracing the SFR. This is, however, before nova explosions in the disk set in. The binary systems need time to evolve in order to host nuclear explosions, leading to a delay between the SFR and the nova rate. In order to investigate the contributions of massive stars and classical novae, they use their 2D chemical evolution model to calculate the amount and distribution of ^{26}Al for two different models: the first one, hereafter Model A, only considered the contribution of mostly massive stars, with minor contributions of type Ia supernovae and asymptotic giant branch (AGB) stars, Model B, additionally included novae as a source of ^{26}Al. Their findings of the ^{26}Al distribution for a region of 15 kpc around the Galactic center at six

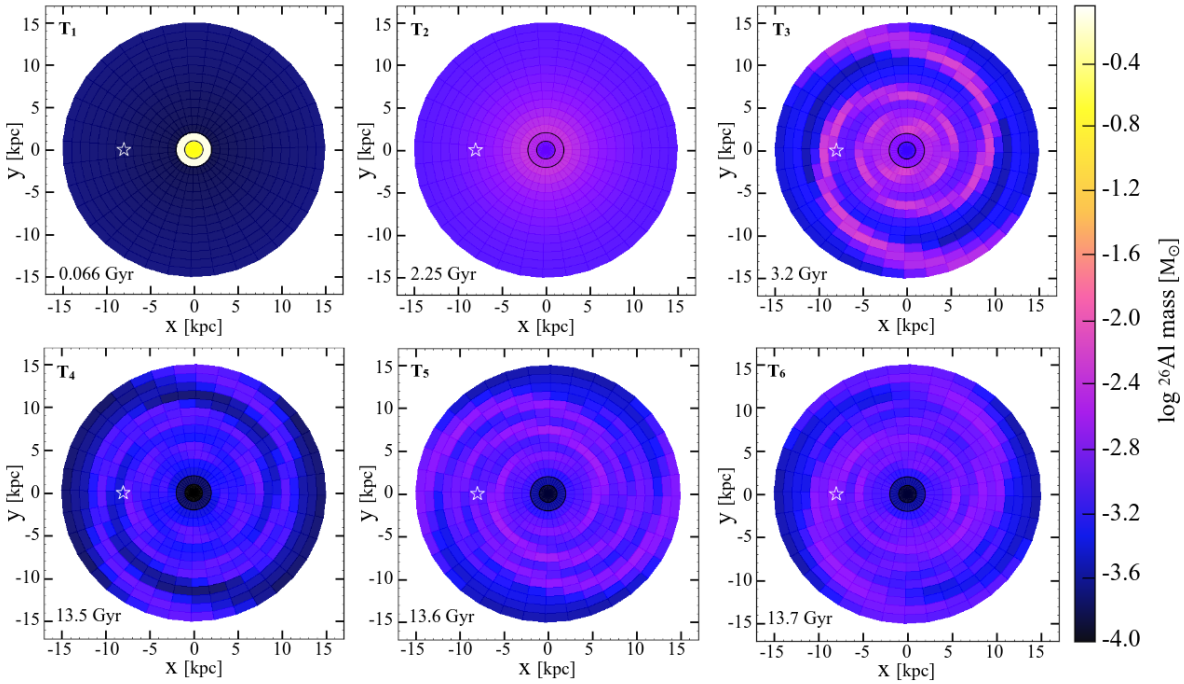

Figure 2.6: Model A: 2D distribution of ^{26}Al mass at six different times. Here only massive stars are considered as contributors. The bulge is not represented and the position of the sun marked with a white star.

different times during the Galactic evolution for both models can be seen in Fig. 2.6 and Fig. 2.7, respectively. For Model A the distribution traces clearly the spiral arms, especially at T_3, when the disk SFR peaked. Even at present day, T_6 the spiral arm pattern is visible. This is even more obvious if compared to the outcome of Model B, where the distribution starts to smear out approximately at the same time as nova explosions set in. At present time, the spiral arms cannot be distinguished anymore.
The total mass of ^{26}Al for the innermost 5 kpc of the Galaxy is given as $M_A = 0.265\,\mathrm{M}_\odot$ and $M_B = 1.028\,\mathrm{M}_\odot$. Their model estimates the mass yielded by massive stars and novae is around four times larger than the amount yielded by massive stars alone, or put differently: massive stars only contribute around 20% of the ^{26}Al mass. Their mass yields are not consistent with measurements, which suggest a total ^{26}Al mass of $2.8 \pm 0.8\,\mathrm{M}_\odot$ [Diehl et al., 2006]. They argue, that the bulge nova rate is probably underestimated, as the dwarf population is of smaller mass and would accrete more matter before explosion.

2.5.2 Very massive stars as sources of ^{26}Al

Another possible source of Galactic ^{26}Al is discussed by Martinet et al. [2022]. They study the stellar wind contributions towards the Galactic ^{26}Al mass of very massive stars (VMS), i.e. stars with initial masses between 150 and 300 $\mathrm{M}_\odot$. They test rotating and

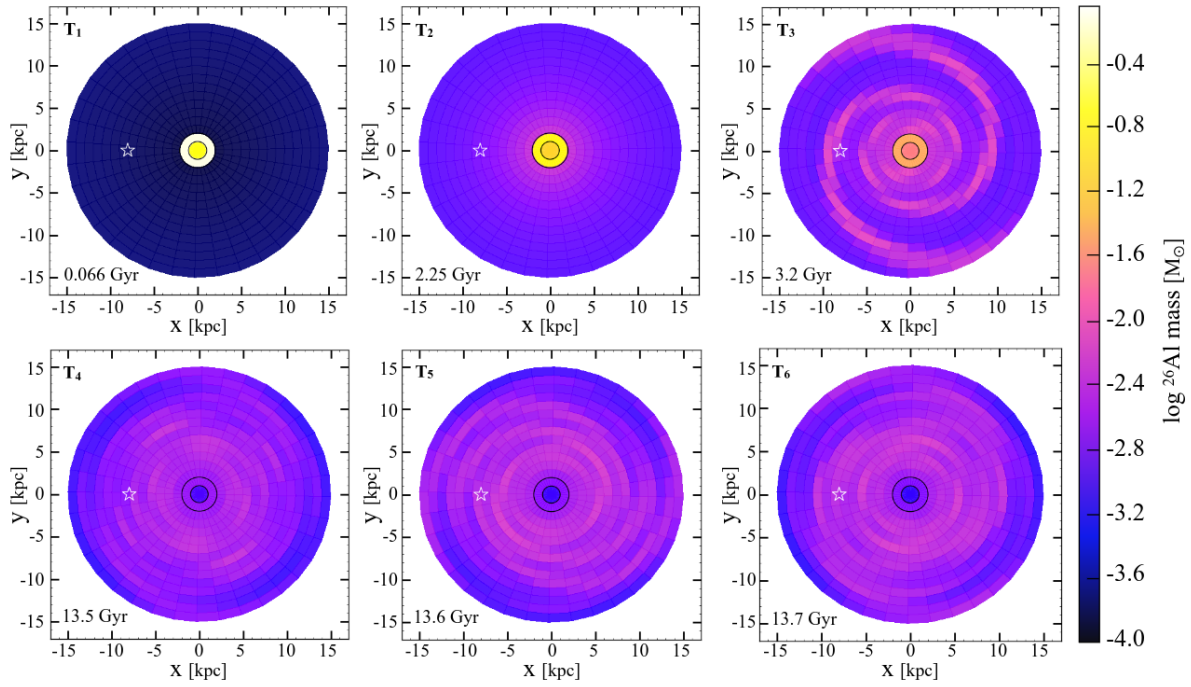

Figure 2.7: Model B: same as Fig.2.6 but this time novae are also considered to produce considerable amounts of ^{26}Al.

non-rotating models for stars with different metallicities.
The quantity ejected by the winds, $Y_{\mathrm{Al26}}^{\mathrm{Winds}}$ is calculated for each model with

$$Y_{\mathrm{Al26}}^{\mathrm{Winds}} = \int_0^{\tau(M,Z,V)} X_{26}^S(M,Z,V,t)\dot{M}(M,Z,V,t)dt \tag{2.9}$$

where $\tau(M,Z,V)$ is the lifetime of a star, V is the initial rotation, $X_{26}^S(M,Z,V,t)$ and $\dot{M}(M,Z,V,t)$ denote the mass fraction of ^{26}Al at the surface and the loss rate as a function of time. The resulting yields are shown in Fig. 2.8 for six different models. For stars of masses below 25 $\mathrm{M}_\odot$ the yields are approximately the same for all models.
Only for initially more massive stars yields exceed 10^{-5} $\mathrm{M}_\odot$. Above this threshold yields increase with initial mass and metallicity. Rotating models almost always show bigger yields, as the rotation enhances the amount of ^{26}Al in the outer star layers. This difference decreases above 60 $\mathrm{M}_\odot$. The only exception is the model with Z=0.006 for masses below 85 $\mathrm{M}_\odot$, where the non rotating model remains at lower effective temperature during He-burning, leading to enhanced mass losses.
They use a normalized IMF

$$\int_{0.07\mathrm{M}_\odot}^{300\mathrm{M}_\odot} \Phi(M)dM = 1 \tag{2.10}$$

in order to interpret $\Phi(M)dM$ as the probability, that a star with initial mass between 0.07 – 300 $\mathrm{M}_\odot$ is formed. They assume that the SFR $\Psi(R)$ was constant for the last

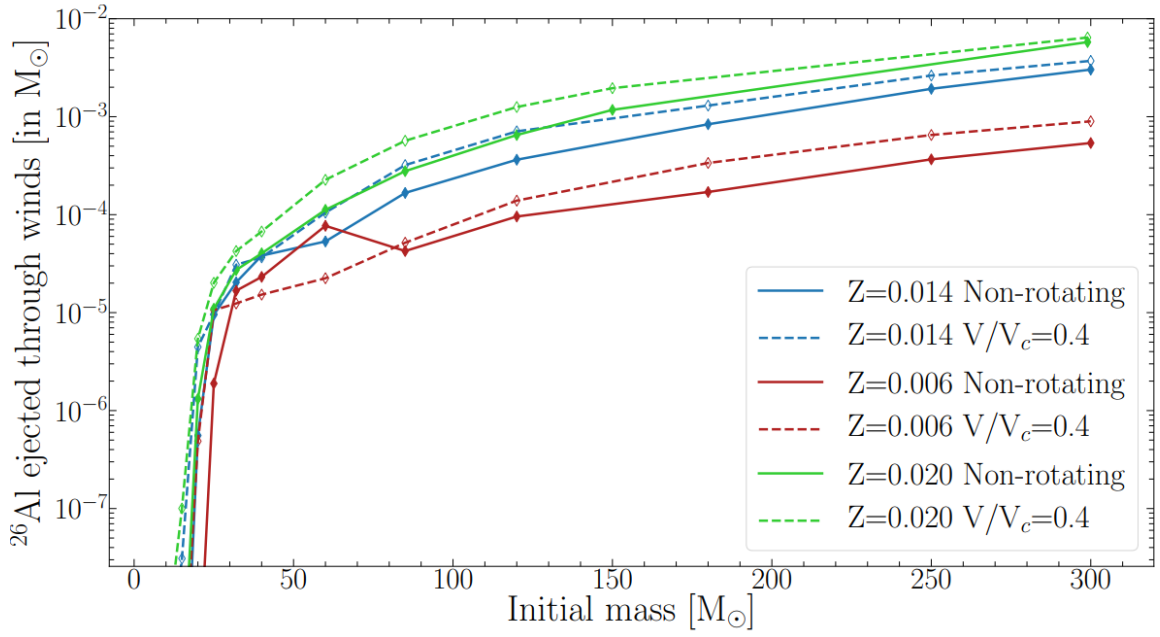

Figure 2.8: Ejected mass of ^{26}Al by stellar winds over the total lifetime of stars with different initial masses, metallicities and rotation rates.

10 Myr and calculate the average mass ejected per star:

$$\bar{Y}^{\text{Winds}}_{\text{Al26}} = \int_{M_{\text{min}}}^{M_{\text{max}}} Y^{\text{Winds}}_{\text{Al26}}(M, Z, V)\, \Phi(M) dM. \tag{2.11}$$

This is used to calculate the contribution of stars as $\Psi(R)\bar{Y}^{\text{Winds}}_{\text{Al26}}$. The total mass per Galactic ring is calculated by integrating over the production rate

$$M_{26} = \int_{R_{in}}^{R_{out}} 2\pi R\, \Psi(R) \bar{Y}^{\text{Winds}}_{\text{Al26}}\, dR. \tag{2.12}$$

They present the distribution of ^{26}Al in rings of 0.1 kpc, by adopting the SFR from Kubryk et al. [2015], a core-collapse supernovae rate of 2 per century, a Salpeter's IMF with α=2.35 and a metallicity gradient from Hayden et al. [2014]. These results are shown in Fig. 2.9. The yields of stars with initial masses over 300 M$_\odot$ have been extrapolated.
They conclude that very massive stars have a significant impact on the global amount of ^{26}Al, and emphasize the need to search for such objects. A rough estimate yields that 2.5 VMS can be expected in a 1 kpc ring around the Sun but, because of stochastic effects, they would probably not be detectable as point-like sources at 1.8 MeV.

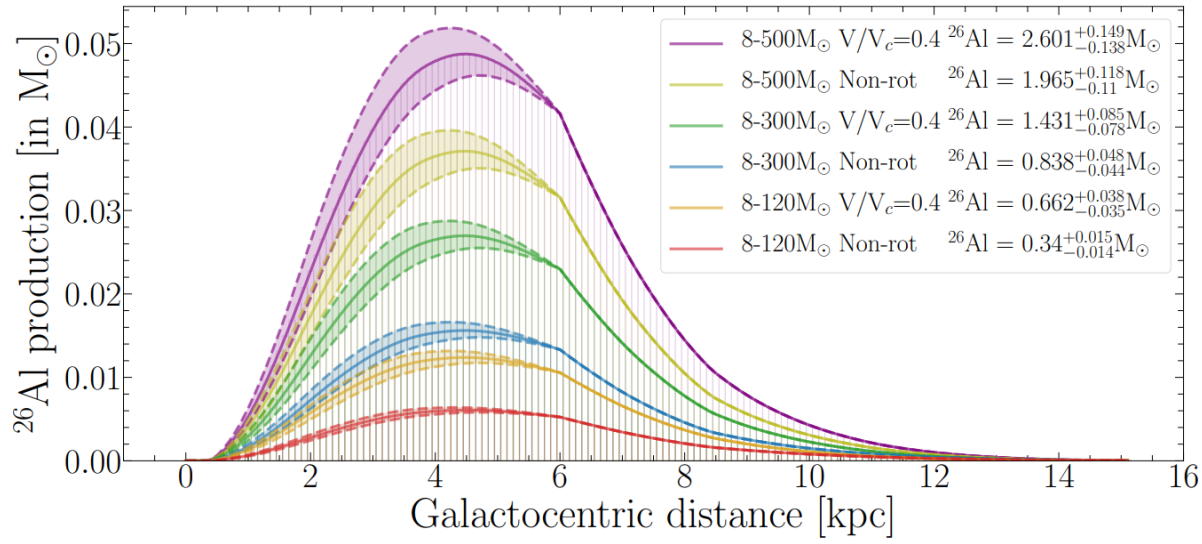

Figure 2.9: ^{26}Al yields of very massive stars for both rotating and non-rotating models compared to yields of only massive stars. All yields for masses above 300 $M_\odot$ have been extrapolated [Martinet et al., 2022].

Chapter 3

Gamma-Ray Line Observations

The most energetic part of the electromagnetic spectrum is the gamma-ray band. The energy range starts at around 100 keV and goes up to orders of more than 10^{12} eV . The Earth's atmosphere is shielding us from high energetic radiation, like gamma-rays. Therefore, if we want to measure them, we have to leave Earth and use satellite telescopes. The 1.8 MeV line associated with ^{26}Al was first predicted to be an observable proof of ongoing nucleosynthesis in the seventies [Ramaty and Lingenfelter, 1977, Arnett, 1977]. In the eighties, it was detected for the first time with the Ge spectrometer on the HEAO-C spacecraft by Mahoney [1984]. Different balloon experiments followed, that already hinted at somewhat extended emission along the Galactic plane. The first all sky survey providing a complete coverage of the Galaxy was achieved in the COMPTEL mission [Oberlack et al., 1996].

3.1 The COMPTEL mission

The **Compton Gamma Ray Observatory** (CRGO) was launched on April 5 1991 as part of the "Great Observatory Program" by the National Aeronautics and Space Administration (NASA). On board were four instruments covering the electromagnetic spectrum in the range of 20 keV to 40 GeV. The imaging Compton telescope COMPTEL was exploring the $0.7 - 30$ MeV range and was used to create the first highly resolved all-sky images of the Galactic 1.8 MeV line.

COMPTEL measured with an angular resolution between $1 - 4\,^\circ$ and a field of view of one steradian For a sphere with radius R the steradian is the solid angle Ω subtended at the center by a spherical cap. The area cut out by the cone is $A = \Omega \times R^2$.[Schoenfelder et al., 1993].

The 1.8 MeV line measured by COMPTEL is clearly distinguished against the background with a difference of more than 13 σ. The all-sky map, Fig.3.6, shows extended emission

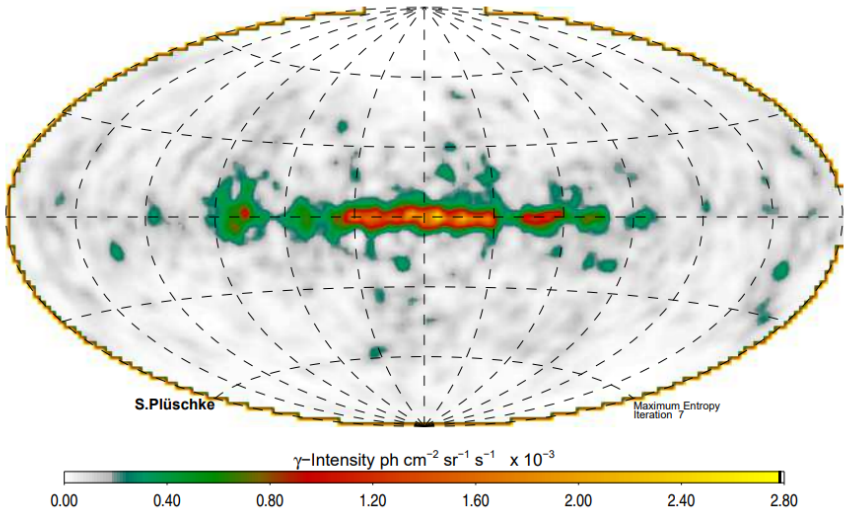

Figure 3.1: This all-sky map of the 1.8 MeV line is the result of 9 years of observations with the COMPTEL telescope [Plueschke et al., 2001].

along the Galactic plane and a clumpy and asymmetric distribution. In model fitting the distribution was best described by an exponential disk with scale radius 3.5 kpc and scale height 180 kpc for the inner radian of the Galaxy [Diehl et al., 1995].

3.2 The INTEGRAL Mission

The **International Gamma-Ray Astrophysics Laboratory** (INTEGRAL) was launched by the European Space Agency (ESA) in 2002. It was originally planned for a mission of 3 years but, due to its huge scientific success, has been extended every two years until the scientific mission ceased in 2025. It will orbit Earth until 2029. To avoid the radiation belts around Earth, and therefore unwanted background noise, INTEGRAL'S orbit is highly eccentric with an initial perigee of 9 000 km and an apogee of 155 000 km. It takes the spacecraft three days for one full orbit, also called *revolution*.

INTEGRAL carries four instruments in order to study a wide energy range. An overview of the spacecraft is given in Fig. 3.2 on the left. The Joint European X-Ray Monitor (JEM-X) and the optical monitor camera (OMC) are monitoring the x-ray and optical energy range while IBIS (Imager on-Board the INTEGRAL Satellite) and the SPI (Spectrometer on INTEGRAL) detector are the main instruments. The components of SPI are shown on the right side of Fig. 3.2. The spectrometer was optimized for high-resolution gamma-ray line spectroscopy in the range of 20 keV − 8 MeV.

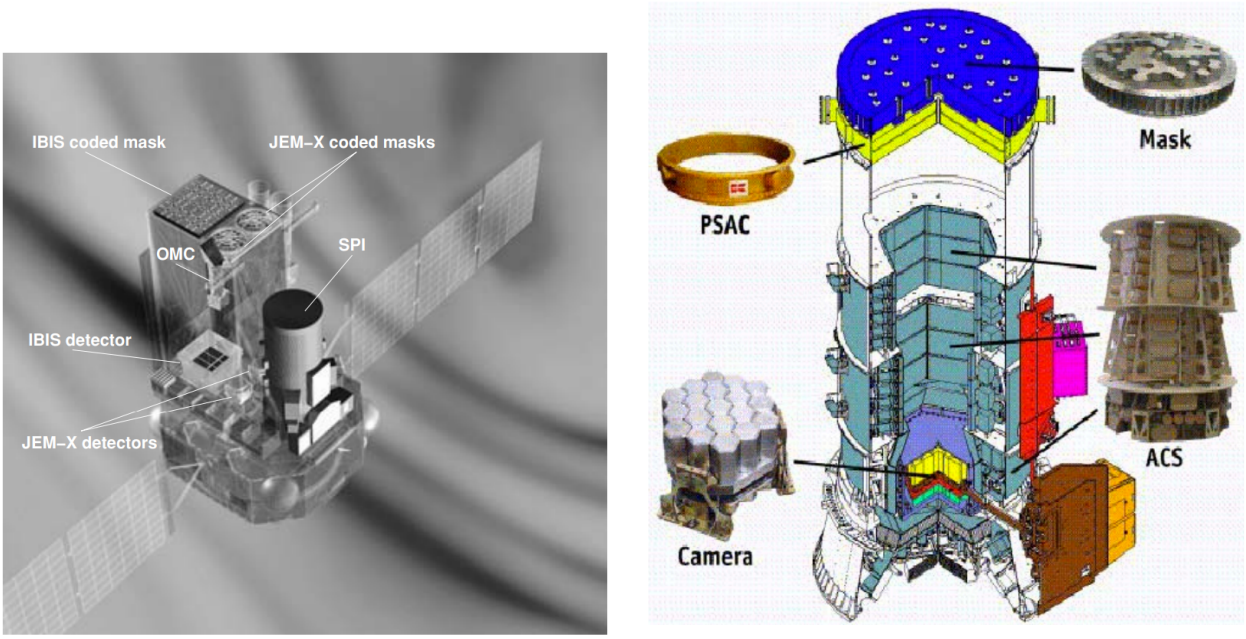

Figure 3.2: An overview of INTEGRAL and its instruments is given on the left hand side [Kretschmar et al., 2005]. The components of the Spectrometer of INTEGRAL (SPI) are shown on the right [Diehl et al., 2018].

3.2.1 The Spectrometer on INTEGRAL

The most important component of SPI is its camera, which consists of 19 individual semiconductor Ge detectors in a hexagonal shape.

In general crystalline material are divided into three categories: insulators, semiconductors and conductors (metals). Their characteristics are defined by the width of the energy gap in the band model. This gap is the energy difference between the free electrons in the material, located in the conduction band and the electrons in the outer atomic shells, laying the valence band. The possible configurations are shown in Fig. 3.3.

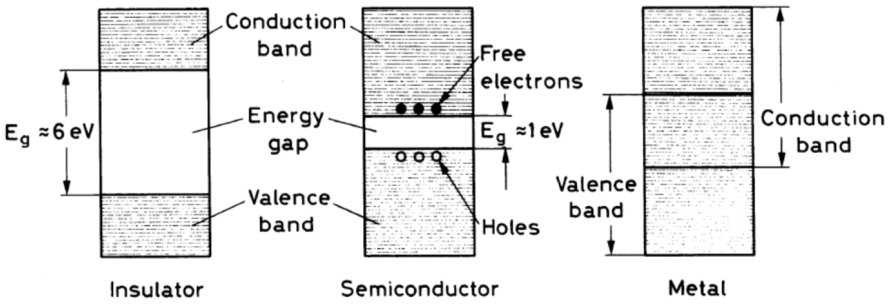

Figure 3.3: Band structure of crystalline materials [Leo, 1994]

For conductors these bands overlap and the electrons can move freely throughout the material. If a electromagnetic field is applied to the crystal, a current can be measured. For an insulator the gap is quite large. The electrons, even if thermically excited, cannot cross the band gap in between. Semiconductors lay in between these two definitions. The energy gap is intermediate in size. At sufficient temperature, some electrons can cross the gap and move from the valence band into the conduction band. They then leave behind an empty place, called hole, which carries a net positive charge. Therefore, a current can be measured if we apply an electric field as both, the hole and the excited electron move, only if some electrons were excited [Demtröder, 2016].
If a semiconductor diode detector is hit by a gamma-ray, several electron-hole pairs are generated because energy is transferred to the Ge material. If an electric field is applied, the electron and the hole move towards the electrodes and can be measured as pulses. The time needed to collect the charges can be adjusted by applying a sufficiently high voltage. To avoid pulses from thermal excitation the detectors need to be cooled down by a cryostat. In a pure crystal the number of holes and electrons are equal. To increase the amount of electrons contributing to the current, small amounts of atoms with one more valence electrons, called donors, are planted into the crystal. This creates excess electrons in the latter, which is easily excited. The crystal is then an n-doped semiconductor. If an atom with one less valence electron is used, a free hole is introduced to the crystal, and we call it p-type material [Leo, 1994].
The detectors in SPI, see Fig.3.4[1], are made from high purity n-type dotted Ge and cover an detection area of $508\,\mathrm{cm}^2$. They are numbered, in order to label them, starting from the central detector at 0 going outwards in an counter clockwise direction. As they can be damaged by radiation, they are regularly annealed by heating them up to 105 °C for one to two days, in order to prevent the cumulative buildup of radiation damage. For operation the cryogenic system cools them down to a temperature of ideally 85 K [Vedrenne et al., 2003].
The mask consisting of 127 hexagonal pixels, is situated at 171 cm above the detection plane. Of these 127 pixels, 63 are opaque to gamma radiation while the other 64 are transparent. The coded mask pattern shows a 120° rotational symmetry and is embedded in a circle with a radius of 360 mm. The opaque pixels are 30 mm thick and absorb more than 90% of the photons over the entire energy range. They are made of a tungsten alloy with a density of $18\,\mathrm{g\,cm}^{-3}$ [Vedrenne et al., 2003]. This mask is shielding parts of the cameras field of view. The photon intensity measured by the detectors therefore depends on the relative position of the detector to the orientation of SPI. Using these shadowgrams the location of a gamma-ray point source can be determined. In Fig.3.5 the shadowgrams

[1] from: INTEGRAL pictures and videos (`http://integral.esa.int/integ_pictures.html`), 24.08.2025

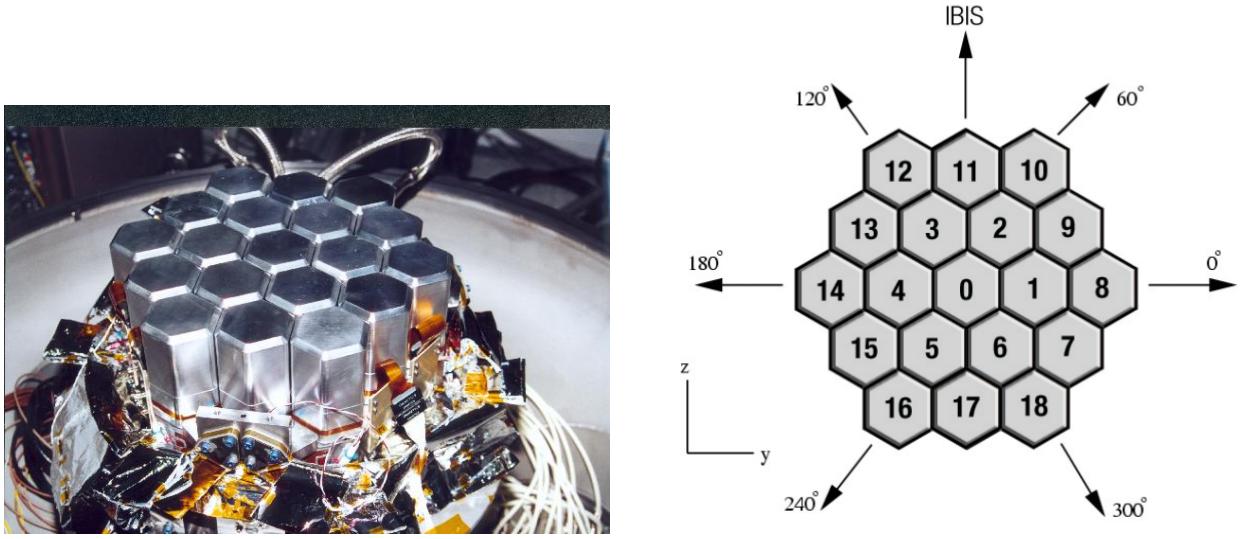

Figure 3.4: The camera of SPI consists of 19 Ge detectors of hexagonal shape (*left*). To distinguish them they are numbered, starting with 0 in the center (*right*) [Diehl et al., 2018].

for a point source are shown for 25 telescope reorientations. SPI is reoriented every 30 min in steps of 2.1°, covering a 5×5 grid around the target [Diehl et al., 2018, Vedrenne et al., 2003].
The anticoincidence shield (ACS) and the Plastic scintillator anticoincidence subassembly (PSAC) are both responsible for reducing background events. The ACS is made of BGO crystals. If it registers an event, a charged particle or a gamma-ray, from outside of the field of view, a veto signal is triggerd for 725 ns. The PSAC is a thin plate directly below the mask. It rejects background coming from interactions with the mask.

3.2.2 The Galactic All-Sky Map by SPI

With more than 10 yr of SPI data the main goal of Bouchet et al. [2015] was to update the COMPTEL view of the ^{26}Al-line. They presented a SPI image that resembled the Maximum entropy Method (MEM) COMPTEL images in order to achieve good comparability. The idea of the Maximum entropy method is that the most probable outcome is the one with maximum entropy (i.e. the least information) Both images are shown in Fig. 3.6 The SPI image shows resolution fixed to 6 ° and gives essentially the same information as the one captured by COMPTEL. It shows extended emission along the galactic plane with strong emission in the inner-Galaxy disk. The SPI map however is more successful in revealing several spots in Cygnus and Taurus region. where the COMPTEL map only shows less clumpy emission. It even shows emission barely detected with COMPTEL at $(l, b) \simeq (161\,^\circ, -3\,^\circ)$ and $(l, b) \simeq (149\,^\circ, 8\,^\circ)$ [Bouchet et al., 2015]. However, artifacts are

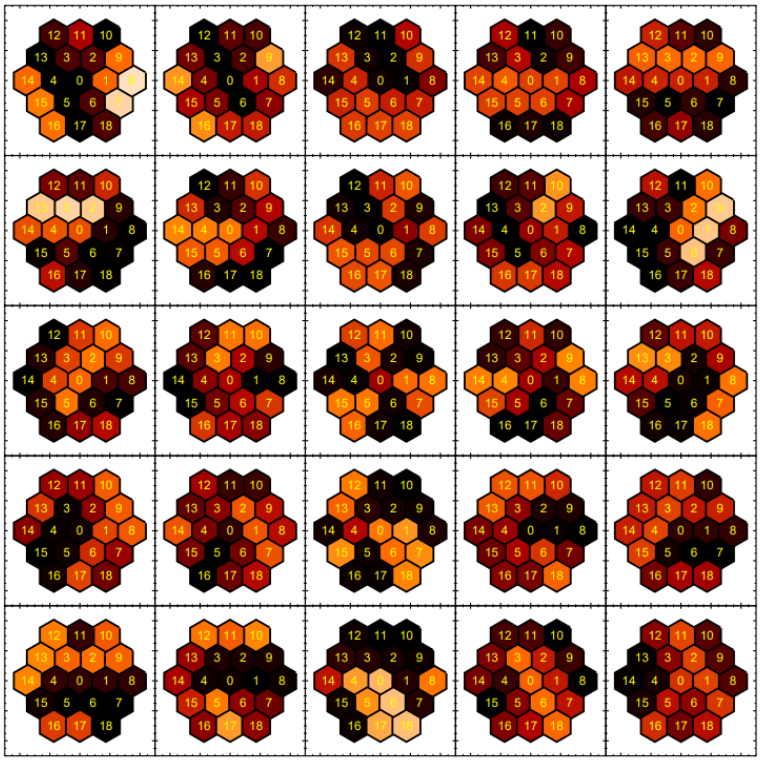

Figure 3.5: Shadowgrams for a point source on axis for 25 telescope reorientations. The color represents the intensity. From Black, shadowed, through red and yellow, to full exposure in white [Diehl et al., 2018].

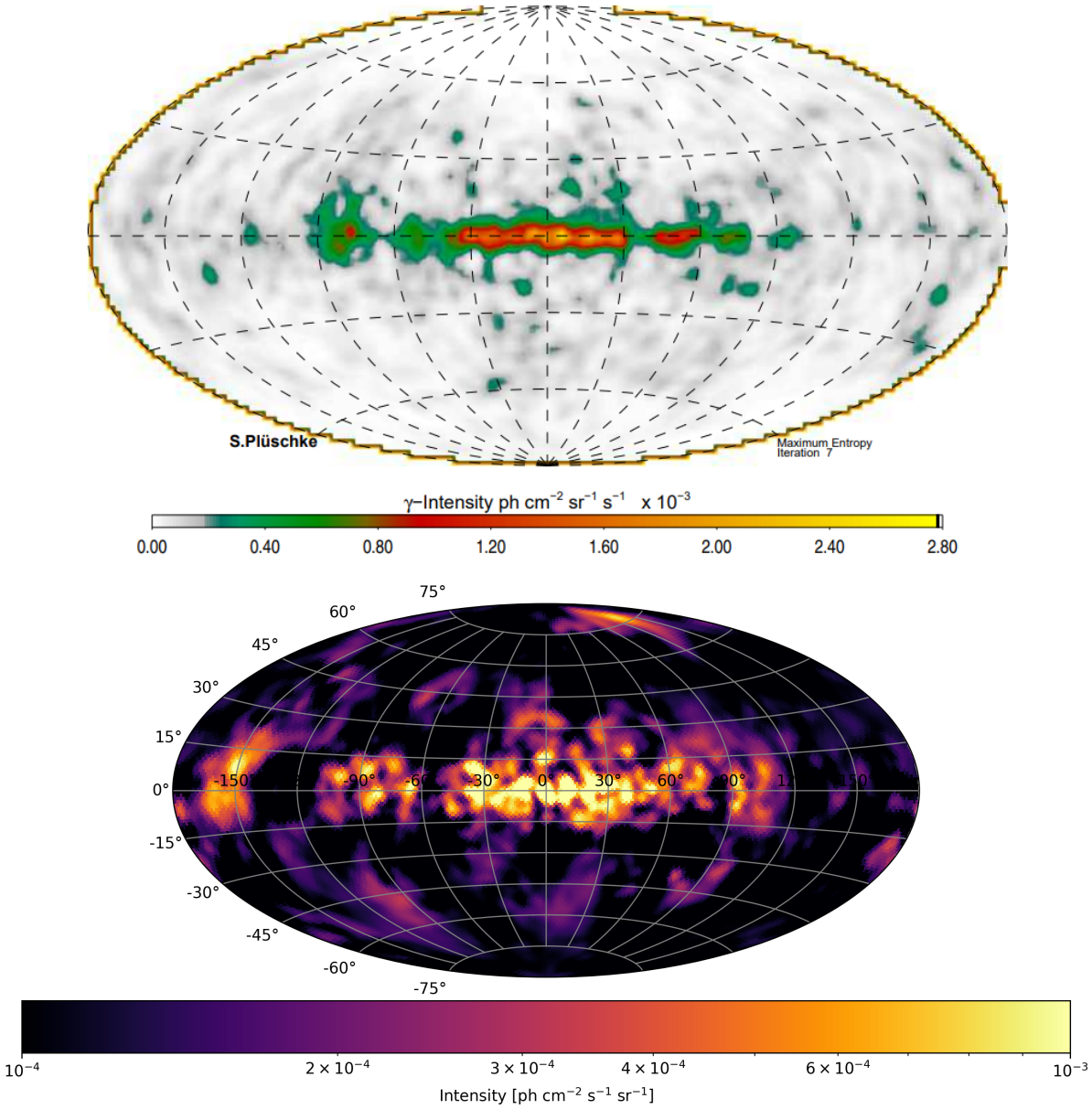

Figure 3.6: Galactic emission at the ^{26}Al line (1805 − 1813keV) as seen by COMPTEL (*left*) [Plueschke et al., 2001] and SPI (*right*) [Bouchet et al., 2015].

also more prone, such as around $(l, b) \simeq (130\,^\circ, 80\,^\circ)$.

Chapter 4

INTEGRAL/SPI data analysis

If the detectors of the SPI camera detect an event, three signals are measured at the front-end electronics: the time of the trigger, the identifier of the detector, and the signal pulse height. The pre-processing of these event data happens at the INTEGRAL Science Data Center (ISDC) in Geneva, Switzerland. There, a first-order energy calibration is performed, calculating the pulse height into keV units and sorting them into count histograms for each detector, and each pointing. This is completed by information about the dead time, and start and end time of each pointing [Diehl et al., 2018].

4.1 Description of the Data set

The data used here are the result of 20 yr INTEGRAL/SPI observations of the entire sky, measuring in the energy range of $1790-1840$ keV in three bins of 15 keV, 8 keV and 27 keV respectively. In the soft gamma-ray energy range all measured spectra are dominated by instrumental background (BG). The BG photons originate mainly from nuclear reactions and continuum-processes due to the exposure of the satellite to cosmic rays. A consistent BG model is therefore needed to analyze SPI data. This is done in a maximum-likelihood framework in the data analysis [Siegert et al., 2019]. The standard analysis tool for SPI data is the OSA software [Courvoisier et al., 2003]. Using OSA, a two step method for spectral fitting is done. First, the photo peak response of the detectors is used to account for the mask pattern on the camera. Using these and the measured data by the individual detectors, a photon flux can be extracted individually per energy channel[Biltzinger et al., 2022].
The structure of the measured data can be written as a function of sky and BG components:

$$d_{i,j,k} = \sum_{l} R_{l;ijk} \sum_{n=1}^{N_s} \theta_n S_{nl} + \sum_{n=N_s+1}^{N_s+N_b} \theta_n B_{n;ijk}. \tag{4.1}$$

Here, $d_{i,j,k}$ is an event count per pointing i, detector j and energy bin k and is written as a sum of sky model components S_n and BG components $B_{n;ijk}$. The sky model components with N_S parameters θ_n represent the photon source intensity per sky direction l. These source intensities are linked to the data space via the response matric $R_{l;ijk}$ [Diehl et al., 2018]. A discussion of the BG can be found in Chapter 4.3

4.2 Statistical Methods

The typical approach for scientific SPI analysis is to compare model predictions with the measured data. Models can either be analytical functions, such as straight lines, broken power laws or Gaussian functions, or more complex convolutions, such as in the case of SPI. However, if only the amplitudes are fitted, such models are called linear models which are straight-forward to implement in fitting algorithms.
This is done by modifying its parameters in order to find the parameter combination that leads to the closest resemblance to the measured data. In no case, however, will the model ever describe real data perfectly as statistical errors occur in measurements. The best fit can be found using different methods, e.g. the maximum entropy as in Chapter 3.2.1. Another approach is based on the idea to find the parameters for which the likelihood to obtain the measured data, plus or minus errors, is maximal, this is called *maximum likelihood method.*

4.2.1 Maximum likelihood method

The counting of photons over time obeys the Poisson statistics. The probability mass function for model m_p is given by

$$P(D|\theta) = \frac{m_p^{d_p} \exp(-m_p)}{d_p!}. \tag{4.2}$$

Where θ are the model parameters and d_p the number of photons per pointing. The number of pointings is called N_{obs} in the following.
The likelihood asks for the probability of measuring the entire data set D, depending on the model parameters. The likelihood for independent counts is the product of the probabilities:

$$\mathcal{L}(D|\theta) = \prod_{p=1}^{N_{\text{obs}}} \frac{m_p^{d_p} \exp(-m_p)}{d_p!} \tag{4.3}$$

It is often more convenient to work with the log-likelihood

$$C(D|\theta) = -2 \ln \mathcal{L}(D|\theta) = -2 \sum_{p=1}^{N_{\text{obs}}} (d_p \ln m_p - m_p - \ln d_p!) \tag{4.4}$$

[Cash, 1979]. As the logarithm is a strictly monotonic function the maximum is preserved. The derivative of the function will be zero at its maximum.

$$\frac{\partial}{\partial\theta}\ln\mathcal{L}(D|\theta) = \frac{\partial}{\partial\theta}\sum_{p=1}^{N_{\text{obs}}}(d_p \ln m_p - m_p - \ln d_p!)$$
$$= \frac{\partial m_p}{\partial\theta}\left(\frac{d_p}{m_p} - 1\right) \stackrel{!}{=} 0 \tag{4.5}$$

This delivers us the best combination of parameters θ.
The likelihood-ratio test, e.g., is a hypothesis test that is used to compare the goodness of fit for two models. It allows to evaluate the statistical significance of a model relative to the null hypothesis. This is done by the *test statistics* (TS),

$$TS = -2(\ln(\mathcal{L}_1) - \ln(\mathcal{L}_\prime)), \tag{4.6}$$

which yields a positive result, that increases with the accuracy of the tested model. TS converges asymptotically to a χ^2 distribution, which allows to calculate the significance, for a one-parameter test by taking the square root Wilks [1938].

4.2.2 The χ^2 Test

For large photon counts, d_p, the Poisson distribution can be approximated by a Gaussian distribution. The goal is to fit a model $y(x,\theta)$, depending on the M free parameters $(\theta_1,\ldots,\theta_M)$, to a set of N data points (x_i, y_i) with standard deviation σ_i. For a Gaussian probability distribution we can calculate the product of probabilities with

$$P \propto \prod_{i=1}^{N}\exp\left[-\frac{1}{2}\left(\frac{y_i - y(x_i,\theta)}{\sigma_i}\right)^2\right]. \tag{4.7}$$

It is again easier to work with the negative of its logarithm, as we are overall, looking for the position of the maximum. We also neglect constants for simplicity

$$\sum_{i=1}^{N}(y_i - y(x_i,\theta))^2. \tag{4.8}$$

If we do not neglect the uncertainties, the equation to minimize is equal to what we call χ^2:

$$\chi^2 = \sum_{i=1}^{N}\left(\frac{y_i - y(x_i,\theta)}{\sigma_i}\right)^2. \tag{4.9}$$

If we take the partial derivative of this, with respect to θ we can find the best fit for our parameters. However, using the degrees of freedom $\nu = N - M$, χ^2 can also be used to

test the goodness of the fit by calculating the reduced χ^2_{red}, defined as

$$\chi^2_{\text{red}} = \frac{\chi^2}{\nu}. \tag{4.10}$$

For a good fit, this should approximately be equal to one.
The χ^2 test is a method to test the statistical significance of the fit. If the best values for the parameters are found, every change to them would lead to an increase of χ^2. The size of the increase is used to define confidence intervals, which give information about the probability of the fit. If only one parameter is modified (i.e. one degree of freedom, $\delta\text{dof} = 1$), the square root $\sqrt{\Delta\chi^2}$ gives the confidence level in units of the standard deviation. In the case of 1σ the confidence interval holds the true values of the parameters in 68.3 % of the time, if the measurement is repeated infinetly often.

4.2.3 Akaike Information Criterion

Using methods like the maximum likelihood method one usually finds, that the best model is the one with the most free parameters. This bares the risk of overfitting the model and an overestimated accuracy. The Akaike information criterion (AIC) [Akaike, 1974] therefore takes into account both, the goodness of fit and the complexity of the model. For a statistical model with k parameters, which are maximized with the likelihood method the AIC value can be calculated by

$$\text{AIC} = 2k - 2\ln(\mathcal{L}). \tag{4.11}$$

This can be used to compare different candidate models to each other. The one showing the minimum AIC value should be preferred. While the logarithmic likelihood assesses the fit quality, the number of parameters act as a penalty by increasing the value.

4.3 Instrumental Background

The spectra measured by SPI are dominated by instrumental BG. This is generally caused by energetic particles interacting with the spacecraft of various origins, like solar flares or regular solar activity during the eleven-year cycle or cosmic rays. BG from the Van-Allen radiation belts, the region in which Earth holds energetic charged particles, mostly originating from the solar wind, are tried to be avoided by shutting off measurements in these regions. When these particles hit the spacecraft, they stimulate radiation processes measured by the instrument. These include e.g. the creation of photons in the energy range of SPI, Bremsstrahlung and nuclear transitions [Diehl et al., 2018].
The BG is composed of a smooth continuum and overlying lines. A large set of these lines are continuously measured and can be used for an characterization of the BG. The line

profiles are modeled as Gaussian functions with an amplitude A_0, the energy position of the center E_0 and the width of the line σ:

$$G(E; E_0, \sigma) = A_0 \exp\left(- \frac{(E - E_0)^2}{2\sigma^2} \right) \tag{4.12}$$

Because the charge collection efficiency degrades between annealings, the line shape is modified by a one-sided exponential depending on the degradation parameter τ:

$$T(E; \tau) = \frac{1}{\tau} \exp\left(\frac{E}{\tau} \right). \tag{4.13}$$

The convolution then gives us a model of the line:

$$\begin{aligned} L(E; E_0, \sigma, \tau) &= (G \otimes T)(E) \\ &= \sqrt{\frac{\pi}{2}} \frac{A_0 \sigma}{\tau} \exp\left(\frac{2\tau(E - E_0) + \sigma^2}{2\tau} \right) \operatorname{erfc}\left(\frac{\tau(E - E_0) + \sigma^2}{\sqrt{2}\sigma} \right). \end{aligned} \tag{4.14}$$

The continuum is modeled by a power law distribution, with a constant scaling factor c_0. It is normalized using the energy center E_M within the region of interest:

$$C(E; \alpha, c_0) = c_0 \left(\frac{E}{E_M} \right)^{\alpha} \tag{4.15}$$

The BG model is fitted for each detector and orbit separately. In Fig. 4.1 it is shown how parts of the spectrum can be represented by an example for the region of the ^{26}Al line [Diehl et al., 2018]. Based on the database of spectral parameters, Siegert et al. [2019] show how to construct a self-consistent BG model for INTEGRAL/SPI that eliminates most of the systematic uncertainties.

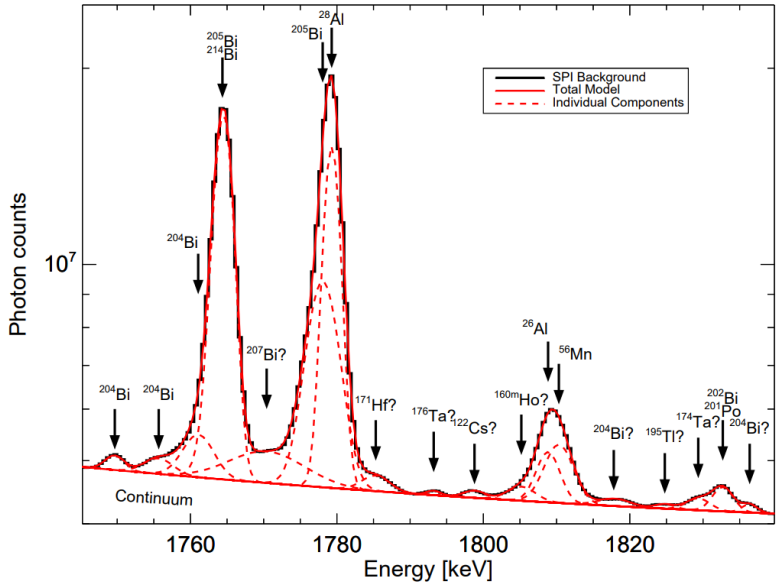

Figure 4.1: BG spectrum decomposed into lines near the 1.8 MeV line of ^{26}Al. Several lines are part of the spectral model. All individual Gaussian models are shown as dashed lines. The corresponding isotopes are identicated when identified [Diehl et al., 2018].

Chapter 5

Astrophysical Modeling

5.1 Spatial Modeling

In order to distinguish the relative contributions of ^{26}Al in the Galaxy, the mass as a function of distance to the Galactic center is to be assessed. In order to do that, several models of the Galaxy are created, with different levels of complexity. These are used to create maps of the sky via *line-of-sight* (LoS) integration.

5.1.1 Line-of-sight integration

Line-of-sight integration is a powerful method to create visualizations of three-dimensional scalar fields. Assuming that the scalar field Φ would emit photons with an intensity proportional to the local numerical value of the scalar, the intensity observed at a certain distance would then be equal to the integral along the line-of-sight.

$$I(\ell, b) = \frac{1}{4\pi} \int_A^B \Phi(x(s, \ell, b), y(s, \ell, b), z(s, \ell, b)) ds \tag{5.1}$$

If the whole object is scanned, a raster image can be calculated [Ruder et al., 1989]. This is illustrated in Fig. 5.1 for two intersecting tori. For the LoS integration over the Galaxy the observer is placed at a 8.2 kpc distance to the Galactic center, the location of the Sun, and integrate over the whole Galaxy (i.e. the limits of integration are $A = 0$ and $B = \infty$)

5.1.2 Galactic models

In total, six different models were used to create sky maps by integrating over their emissivity profile. They consist of double-exponential and double-Gaussian Galactic disks, as well as, combinations of them, i.e. Galactic disks with exponential scale radius and Gaussian scale height and Galactic disks with Gaussian scale radius and exponential scale

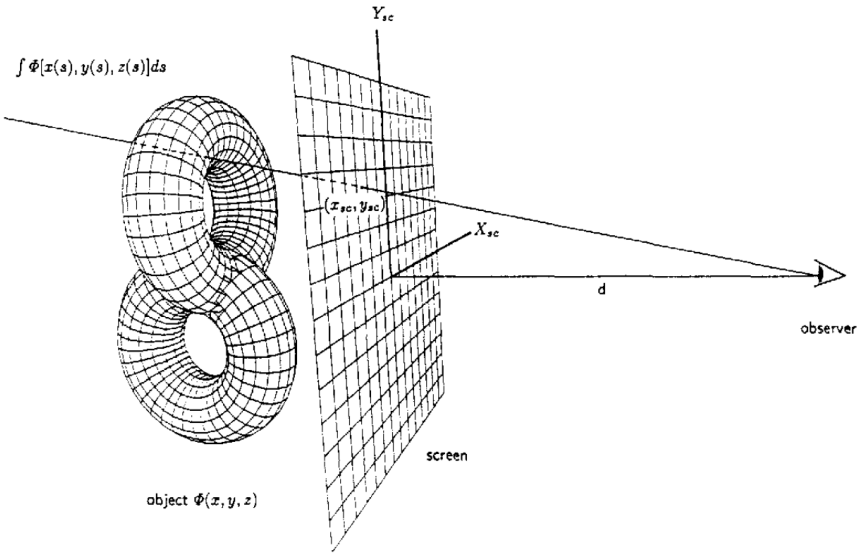

Figure 5.1: Visual representation of the line-of-sight integration method. The intensity for each pixel on the screen is proportional to the integral through the object along the line of sight [Ruder et al., 1989].

height. Finally, two more complex models were tested that considers the spiral-arms of the Galaxy. The spiral distribution was mimicked by tracking the stellar and dust emission in the Milky-Way as seen at different ranges of the electromagnetic spectrum, namely 360 nm (ultraviolet; UV), 450 nm (optical; O) or 800 nm (infrared; IR) and shown in Fig. 5.2.Robitaille et al. [2012] work also focused on the diffuse emission of polycyclic aromatic hydrocarbons, which are expected to depend on the distribution of massive stars. Because of this, their model may also connects to the distribution of massive stars. This model is applied in order to test a model showing more physical properties than the ones described above. We separate it by wavelengths into two parts and create maps following their distribution in the IR spectrum and the OUV. Example maps of all models are shown in Fig. 5.5. For the first models considering exponential or Gaussian distributions, different combinations of the scale radius, R_E, and the scale height, z_E can be tested in order to find a best fit model. The emissivity profiles for these models can be found in Table 5.1, where $R_{x,y}$ denotes the Galactocentric distance. They consider the spatial emissivity $\rho(x, y, z)$ of the ^{26}Al line, which is depending on the luminosity

$$L_0 = \frac{M_{26} p_{26}}{m_{26} \tau_{26}} \tag{5.2}$$

as a function of different isotope properties: the persistent ^{26}Al mass M_{26}, the probability to emit a photon at 1.8 MeV after decay $p_{26} = 0.997$, the isotope mass $m_{26} = 26$ u and the lifetime $\tau_{26} = 1.04$ Myr.

It is normalized by the *effective volume* of the model, also given in Table 5.1. These profiles form the input for the LoS integration, producing model sky maps, that can be

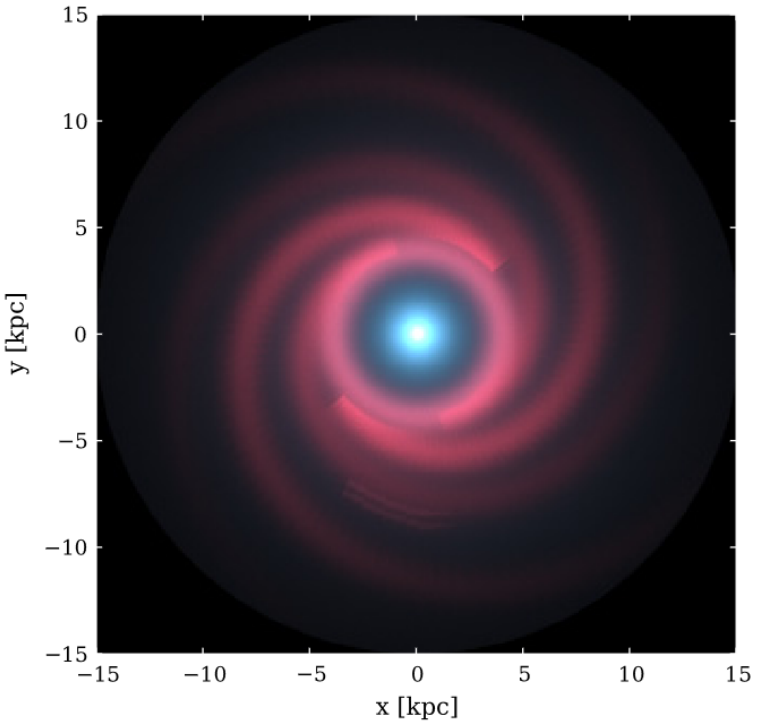

Figure 5.2: Color coded view of the Galaxy model by Robitaille et al. [2012]. They show results measured with the infrared camera IRAC on board of the *Spitzer Sace Telescope* at different wavelenghts: 3.6 μm (blue), 4.5 μm and 8.0(green) μm (red).

Disk model	**Density**	**Effective Volume**
Double exponential	$\rho(x,y,z) = \frac{L_0}{4\pi R_E^2 z_E} \exp\left(\frac{-\lvert z\rvert}{z_E}\right) \exp\left(\frac{-R_{x,y}}{R_E}\right)$	$4\pi R_E^2 z_E$
Double Gaussian	$\rho(x,y,z) = \frac{L_0}{(2\pi)^{3/2} R_E^2 z_E} \exp\left(\frac{-z^2}{2z_E^2}\right) \exp\left(\frac{-R_{x,y}^2}{2R_E^2}\right)$	$(2\pi)^{3/2} R_E^2 z_E$
Exponential scale radius, Gaussian scale height	$\rho(x,y,z) = \frac{L_0}{(2\pi)^{3/2} R_E^2 z_E} \exp\left(\frac{-z^2}{2z_E^2}\right) \exp\left(\frac{-R_{x,y}}{R_E}\right)$	$(2\pi)^{3/2} R_E^2 z_E$
Gaussian scale radius, exponential scale height	$\rho(x,y,z) = \frac{L_0}{4\pi R_E^2 z_E} \exp\left(\frac{-\lvert z\rvert}{z_E}\right) \exp\left(\frac{-R_{x,y}^2}{2R_E^2}\right)$	$4\pi R_E^2 z_E$

Table 5.1: Density profiles for different models of the Galaxy. The effective volume is used to normalized the emissivity

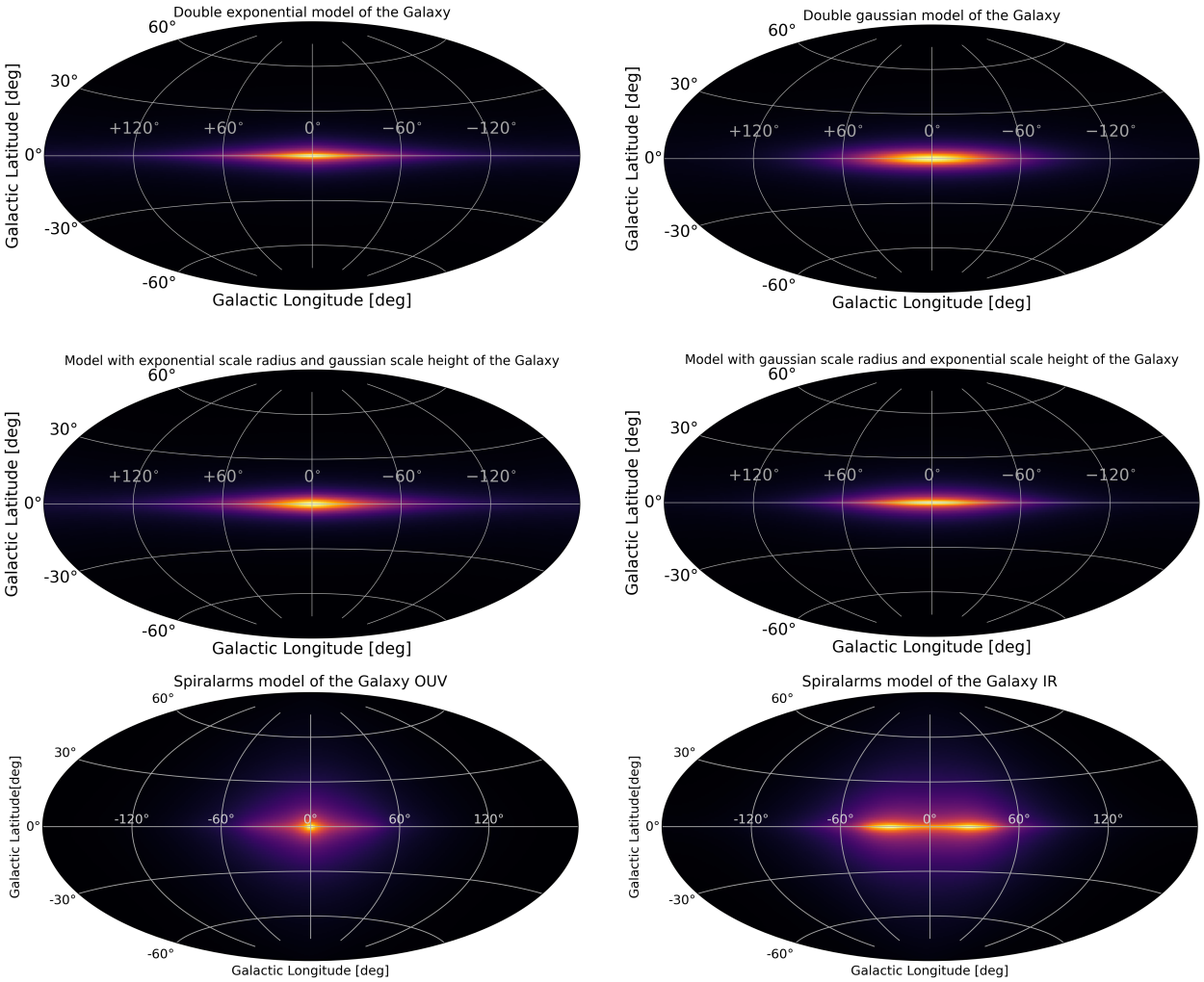

Figure 5.3: Example maps of the Galaxy for different models. The flux is given in arbitrary units from yellow, maximum flux, to black, zero flux. Models with Gaussian and/or exponential parameters were calculated with the same scale values of $R_E = 5.0\,\mathrm{kpc}$ and $h_E = 0.6\,\mathrm{kpc}$.

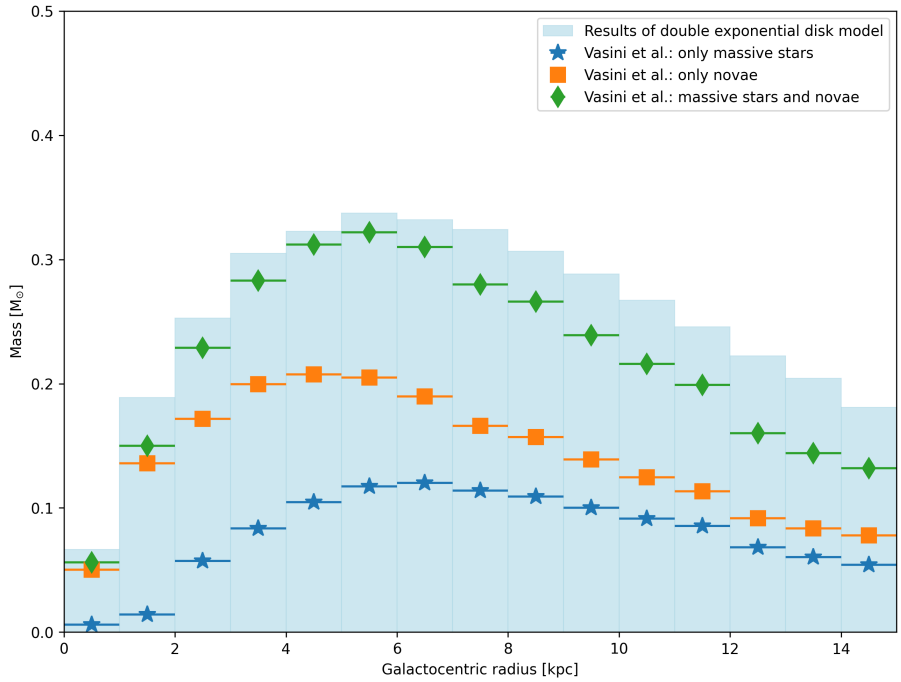

Figure 5.4: Comparison of the mass values predicted by Vasini et al. [2025] and geometric distribution of masses predicted by the double exponential model. The mass originating only from classical novae (orange) and only from massive stars (blue) sum to the total prediction (green). The blue histogram shows the masses inside rings with fixed scale height and radius up to 15 kpc in 1 kpc steps.

convolved with the *SPI instrument response function* (IRF), which accounts for the coded mask, detector response, and the point spread function. The resulting predicted detector counts are compared to actual measured photons, and a likelihood fit is done to adjust the model intensity by *spimodfit* [Strong et al., 2005] within the OSA software [Courvoisier et al., 2003].

Fig. 5.4 shows the geometric distribution of masses predicted by the a double exponential model compare to the mass values calculated with the theoretical GCE model of Vasini et al. [2025]. The predicted mass of ^{26}Al was calculated from the model density $\rho(x, y, z)$, in cylindrical coordinates, as an integral over the ring volume:

$$M_{26} = \int_{R_{\text{in}}}^{R_{\text{out}}} \int_{-\infty}^{\infty} \int_{0}^{2\pi} \rho(R, z)\, R\, dR\, dz\, d\phi\, m_{26}\, \tau_{26}. \tag{5.3}$$

The blue histograms show the mass inside rings with fixed scale radius and height for the innermost 15 kpc of the Galaxy in 1 kpc steps. The model of Vasini et al. [2025] predicts the mass contributed by classical novae and massive stars to peak at different distances towards the center. Additionally, the rise for the novae curve is much steeper. This will allow us to calculate the actual contributions of sources after the best spatial model is found.

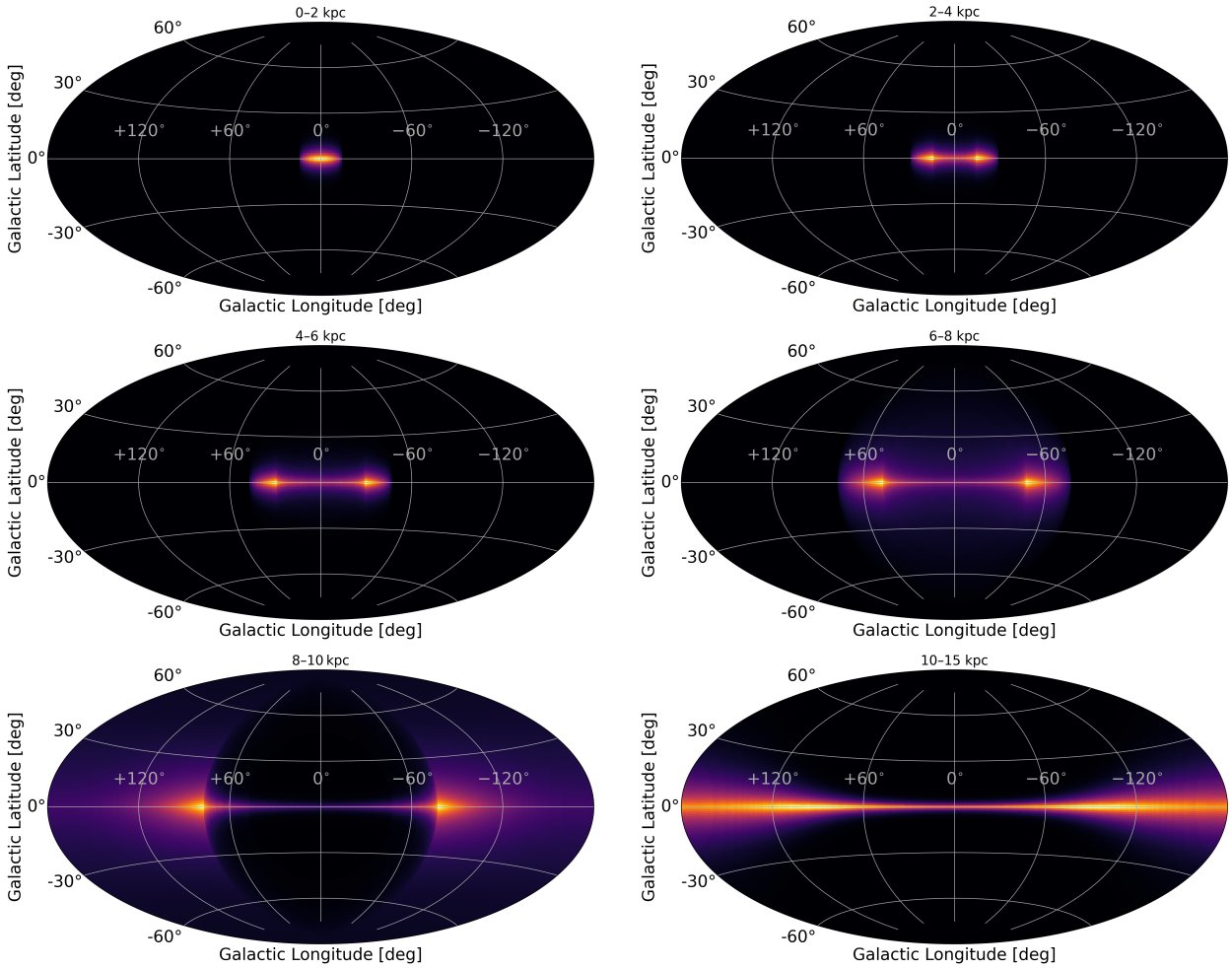

Figure 5.5: Example maps of a cut Galaxy for a double exponential model with scale values of $R_E = 5.0\,\mathrm{kpc}$ and $h_E = 0.6\,\mathrm{kpc}$. The flux is given in arbitrary units from yellow, maximum flux, to black, zero flux. Here, the Galaxy was cut into rings from 0–2 kpc, 2–4 kpc, 4–6 kpc, 6–8 kpc, 8–10 kpc, and 10–15 kpc of Galactocentric distance.

To predict the Galactic distribution of ^{26}Al a single model falls short. We therefore separate the Galaxy into concentric rings and fit all of them simultaneously. This yields the Galactic distribution of ^{26}Al. If we consider the total model Mass M to be a linear function, with parameters a_N and a_MS, of the masses originating in massive stars and classical novae, M_MS and M_N respectively,

$$M = a_\mathrm{N} \times M_\mathrm{N} + a_\mathrm{MS} \times M_{MS} \tag{5.4}$$

we can fit it towards the mass distribution predicted by a GCE via a χ^2-test. To cover a big enough parameter space, we test 100 values between 0-500 % for a_N and a_MS. For $a_\mathrm{N} = a_\mathrm{MS} = 1$, M equals the predictions of the tested model. Then, the total mass, $M = 1 \times M_\mathrm{N} + 1 \times M_\mathrm{MS}$, is the direct sum of both model components. This is equal to 100 % contribution of each source. In order to determine the distribution relative to

	Model M_N	Model M_{MS}
Model 1	Classical Novae [Vasini et al., 2025]	massive stars [Vasini et al., 2025]
Model 2	Classical Novae [Vasini et al., 2025]	non-rot VMS<300 $M_\odot$[Martinet et al., 2022]
Model 3	Classical Novae [Vasini et al., 2025]	rot VMS<300 $M_\odot$[Martinet et al., 2022]
Model 4	Classical Novae [Vasini et al., 2025]	non-rot VMS<500 $M_\odot$[Martinet et al., 2022]
Model 5	Classical Novae [Vasini et al., 2025]	rot VMS<500 $M_\odot$[Martinet et al., 2022]

Table 5.2: Combination of Models that are to be tested in a χ^2 test in order to determine the relative contribution of M_N and M_{MS} to Galactic ^{26}Al.

the source and not the model, the parameters then have to be normalized. The relative contribution of novae are calculated by:

$$a_{\rm rel} = a_{\rm N,min}\frac{M_{\rm N}}{M_{\rm bf}} \tag{5.5}$$

where we consider the best fit mass $M_{\rm bf}$

$$M_{\rm bf} = a_{\rm MS,min}M_{\rm MS} + a_{\rm Nmin}M_{\rm N}. \tag{5.6}$$

This is just Eq. 5.4 for the parameter combination at minimum χ^2. After normalization, the parameters are corresponding to the relative contribution of novae and massive stars. Their uncertainties can be determined by the distance to the edge of the confidence interval. We test five different models, considering the GCE by Vasini et al. [2025] as is, but also combining it with the model of Martinet et al. [2022] in order to account for possible contributions of VMS to Galactic ^{26}Al, that would diminish any novae contributions. The composition of these models, with respect to Eq. 5.4, are given in Tab.5.2.

5.2 Dissecting the Galaxy

To determine the mass distribution as a function of Galactocentric distance, the Galaxy is cut into multiple rings. This leads to a better radial resolution for smaller pieces but increases uncertainties and correlations between component. The number of rings is decided by the size of the error bars for the models. The idea is to find the model with the smallest uncertainties but the most information.
For each ring a sky map is generated by LoS-integration, yielding a model flux map for the initial reference luminosity $L_0 = 1.42 \times 10^{42}\,\mathrm{s}^{-1}$, which corresponds to an ^{26}Al mass of $M_{26} = 1\,M_\odot$. These maps are then fitted simultaneously towards the raw INTEGRAL/SPI data and yields a flux value.
The observed flux can be directly translated into the number of decaying nuclei. The amount of photons released per unit time corresponds to the luminosity L, see Eq.5.2.

The flux, in turn, is defined as the luminosity per unit area, at the observer's position. After fitting, the fitted flux for each component can be written as

$$F_{\text{fit}} = F_{\text{norm}} \frac{L_{\text{fit}}}{L_0}. \tag{5.7}$$

Because the luminosity is directly proportional to the mass, and L_0 corresponds to M_0, the fitted mass components can be then calculated directly:

$$M_{\text{fit}} = M_{\odot} \frac{F_{\text{fit}}}{F_{\text{norm}}}. \tag{5.8}$$

The corresponding uncertainty is calculated by Gaussian error propagation:

$$\sigma_{M_{\text{fit}}} = \sqrt{\sigma^2_{F_{\text{norm}}} \left(\frac{M_{\odot}}{F_{\text{norm}}} \right)^2} \tag{5.9}$$

5.3 Systematic Uncertainties and Model Limitations

All physical measurements are subject to statistical uncertainties. Photon counts are Poisson distributed as SPI counts every photon per energy bin per detector. In these cases the uncertainty depends on the total amount of counted events. The measurement becomes more certain, the more photons are measured. This means, in the case of, regions showing small flux are less well-known than brighter areas of the sky. If the sample of measured photons is too small, the statistical methods applied may not be appropriate. In Section 4.2.2, the asymptotical approach of the Poisson towards the Gaussian distribution is introduced for large enough photon counts. If not enough photons are measured, statistical criteria as the χ^2 test lack validity. While the 1.8 MeV line is quite strong, this might become relevant if the are of interest is too small, e.g. very fine concentric rings.

In general, systematic uncertainties dominate for strong signals. The angular resolution of SPI ($\sim 2-3°$) is insufficient to adequately image finer structures, such as small regions of star formation in the Galaxy. These structures are effectively blurred together and cannot be distinguished individually. Consequently, two different models might yield different results in terms of flux but show the same likelihood, because SPI's resolution is to coarse to detect the difference of these models.

The choice of smooth parametric models, like an exponential models is not unique to this thesis. The amount of young massive stars decreases exponentially with radius, which indicates a similar distribution for ^{26}Al and they allow for stable fits. However, they do not account for the actual complexity of the Milky Way. They neglect any asymmetries and the spiral arm pattern. In the case of ^{26}Al emission, there is evidence that previously determined scale height values of the entire Galaxy are significantly biased

by local foreground. A single parameter model lacks to track the bimodal distribution of scale heights (for a fixed scale radius) apparent by SPI measurements [Pleintinger et al., 2019]. This is why the spiral model by Robitaille et al. [2012] is also tested. This is a closer match in terms of morphology even though it still contains some simplifications. However, this model is not tracing ^{26}Al directly. It models stellar and dust infrared emission. While regions of large dust density are found in the center of the spiral arms and are associated with the formation of young stars, the distribution of ^{26}Al is shifted away from these areas in front of the spiral arms. These shift are because in the time needed to fuse ^{26}Al, its host star has already moved away from the center of the spiral arms. The spiral arm model used here might therefore only loosely connect to the ^{26}Al distribution in the Galaxy and not describe the spiral arm pattern in the gamma-ray energy range of 1.8 MeV.
When determining the contributions by a χ^2 test, we compare our model results to theoretical predictions. Those are the result of state of the art Galactic Models but not necessarily a true description of the actual Galaxy. Vasini et al. [2025], e.g., underestimate the total amount of ^{26}Al by a factor of almost two for the innermost 5 kpc of the Galaxy. While the total amount of mass is not effecting the results of the χ^2 test directly, as it only depends on the relative distribution, this might change the relative composition of the model. This is not accounted for in the test itself, as only the uncertainties of the tested model is used as an parameter, while the prediction is treated as free of uncertainties.

Chapter 6

Results

6.1 Resolving the 1.8 MeV line

In order to investigate the 1.8 MeV line, the data set was rebinned from 0.5 keV bins into three separate bins from 1790–1805 keV (continuum), 1805–1813 keV (line) and 1813–1840 keV (continuum). The flux per bin is plotted in Fig. 6.1. In order to estimate the significance of the line, a TS test was performed. This yields an significance of 26.8 σ of the line against the continuum. For each *spimodfit* run, the number of free parameters can be increased by readjusting the background more often. This of course increases the log-likelihood of the fit, see Fig. 6.2 on the left. In order to find the best background model, we perform multiple fits with adjusted background, and calculate the AIC for each of them. The results can be seen on the right hand side of Fig. 6.2. This shows, that an renormalization of the background every two INTEGRAL orbits is sufficient.

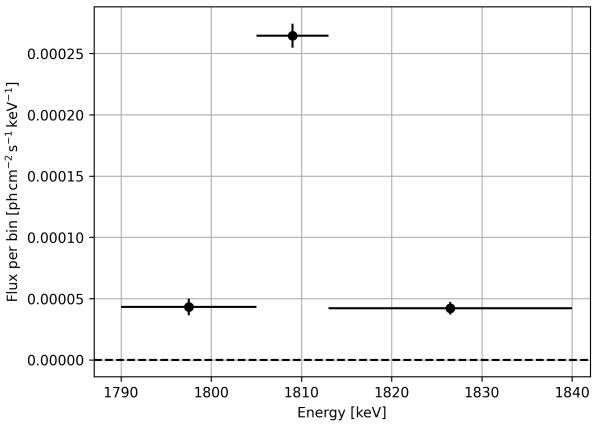

Figure 6.1: Differential Flux measured by INTEGRAL/SPI for energies between 1790–1840 keV in three bins representing continuum emission and the ^{26}Al-line at 1.8 MeV. The line stands out at 26.8 σ against the continuum.

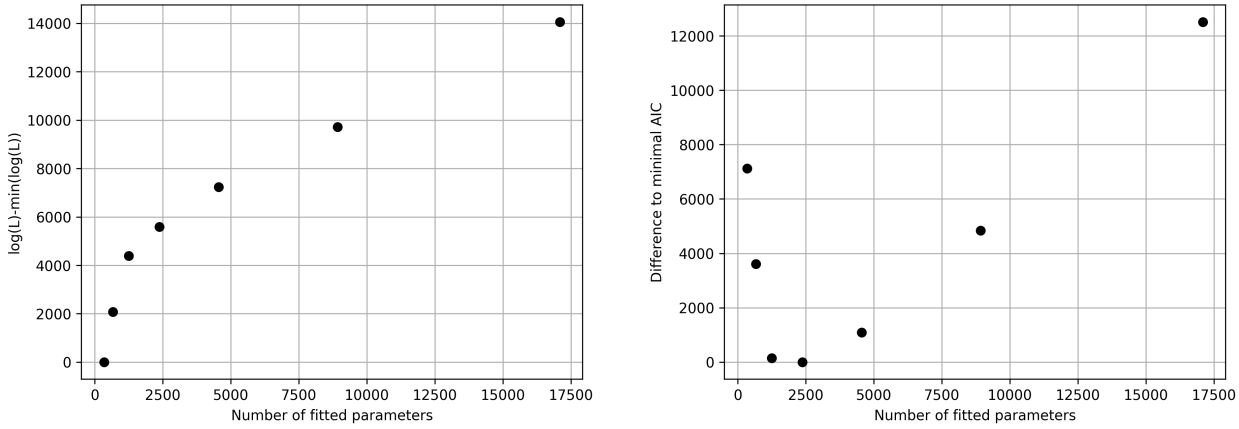

Figure 6.2: The absolute value of the log-likelihood increases with the number of parameters (*left*). Therefore, multiple fits with growing numbers of fitted parameters are done, to find the model that shows the minimal AIC.

R_E [kpc]	h_E [kpc]
4.0	0.4
5.0	0.6
5.5	0.7
6.0	0.8
7.0	1.0

Table 6.1: All global models were tested for these combinations of scale values.

6.2 Finding the best Galactic model

In order to find the best description of the Galaxy we test different spatial models. The goodness-of-fit is determined by the maximum log-likelihood method in order to directly compare the models with each other.

6.2.1 A global model

First, a global double exponential model was probed. In order to estimate some systematic uncertainties, in addition to the statistical uncertainties from the maximum likelihood fit, we test different combinations of scale values, R_E and h_E . Pleintinger et al. [2019] present good fit value combinations for a double exponential disk model. For each model, five combinations of values are tested, given in Table 6.1. The sky maps are fitted to our data set, using the log-likelihood as indicator for the relative quality of the fit. Additionally the corresponding masses for each map were calculated. The results are shown in Figure

Model	Mass of ^{26}Al [$M_\odot$]	Uncertainty from Poisson only [$M_\odot$]	Uncertainty from Shape[$M_\odot$]
Double Exponential	4.57	$\pm$0.16	$^{+0.43}_{-1.17}$
Double Gaussian	2.95	$\pm$0.10	$^{+0.6}_{-0.5}$
Exponential Radius + Gaussian Height	4.36	$\pm$0.18	$^{+0.44}_{-0.36}$
Gaussian Radius + Exponential Height	4.01	$\pm$0.14	$^{+0.36}_{-0.4}$
Spiral-arms as seen in OUV	21.67	$\pm$ 0.79	
Spiral-arms as seen in IR	23.37	$\pm$0.84	

Table 6.2: Total mass of ^{26}Al for global models of the Galaxy. The uncertainties from Poisson only are calculated by Gaussian error propagation of the flux uncertainties. Another approach is to calculate the uncertainties from the shape of the model by considering $\Delta \log \mathcal{L} = 0.5$ around the best fit value.

6.3. The masses for the spiral models are not shown in the plot, as they exceed the others by a fair amount. Their values, as well as the mass for the best fit per model are given in Tab. 6.2. All analytic models show a best fit values for combination $R_E = 5.0\,\mathrm{kpc}$, $h_E = 0.6\,\mathrm{kpc}$. The best global model is given by an double exponential approach. The double gaussian map falls short, compared to the other geometrical models. The spiral-arm models show by far the worst relative log-likelihood, being disfavoured by $\Delta \log \mathcal{L} = 26$, for the IR model, and $\Delta \log \mathcal{L} = 30$, in the OUV case. This was to be expected as the spiral arm model used is only loosely connected to what we want to probe and was discussed in Chapter 5.3 in detail. These results obtains an adequate starting point for selecting models when the Galaxy is fitted by the six-component models.

6.2.2 The best Model for a dissected Galaxy

In order to find the best size of rings, the Galaxy was cut gradually into sections of smaller size. At first, it was dissected into two parts, with a 8 kpc width. These were then cut in half again into rings of 4 kpc, then again into eight 2 kpc rings. Finally 16 1 kpc rings were fitted. The resulting differential fluxes for a double exponential model with $R_E = 5.0\,\mathrm{kpc}$, $h_E = 0.6\,\mathrm{kpc}$ are shown in Fig. 6.4. According to the increase of the size of the uncertainties, the Milky Way is cut in rings of 2 kpc up to a distance of 10 kpc from the center. Given that the uncertainties become orders of magnitude larger

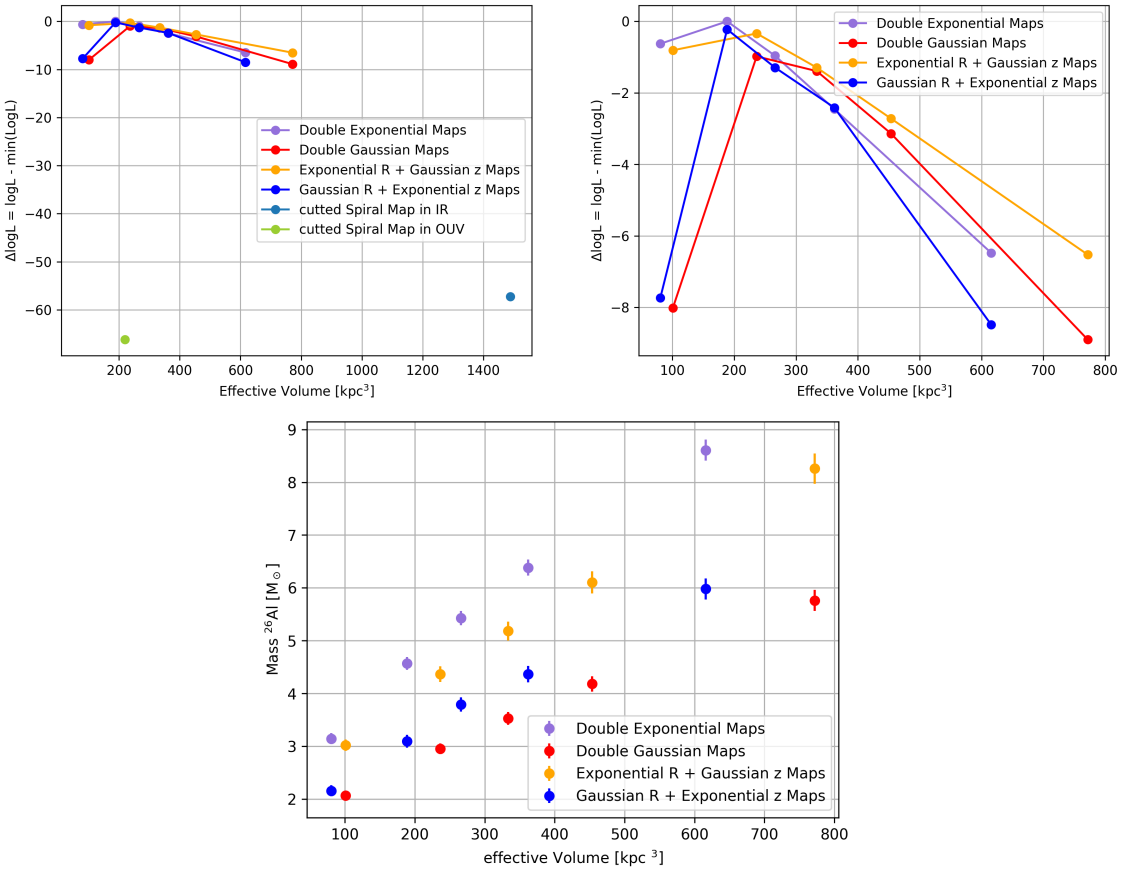

Figure 6.3: Plotting the log-likelihood of the tested models as a function of effective volume (*upper panels*). Note that the effective volume is given in Table 6.1, so that different combinations of R_E and h_E can lead to the same volume but different likelihoods. Due to computational constraints, we use V_{eff} as a summary variable. Both spiral arm models show log-likelihoods way below the best fit and are deemed rather unlikely. The same plot is shown again without these, in order to show the distribution of the other models. All other models show minimal log-likelihood For R_E= 5.0 kpc and h_E = 0.6 kpc. The corresponding masses for the analytic models can be seen in the lower panel. For the best fit, model suggestions lay in between $(2.95 \pm 0.10)\,\mathrm{M}_\odot$ and $(4.57 \pm 0.16)\,\mathrm{M}_\odot$.

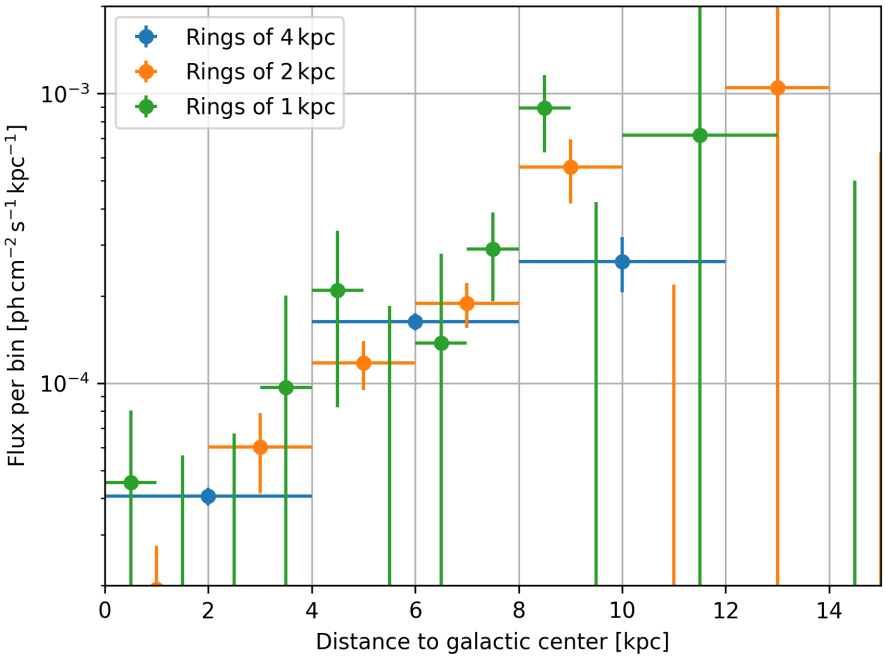

Figure 6.4: Flux distribution of the 1.8 MeV line depending on Galactocentric radius for a double exponential Model.

R_E [kpc]	h_E [kpc]
4.0	0.4
5.0	0.4
5.0	0.6
5.5	0.7

Table 6.3: All global models were tested for these combinations of scale values.

than inside the Solar circle, we use one 5 kpc ring from 10–15 kpc. The Galactic size of 15 kpc was adjusted to the available GCE model calculations of Vasini et al. [2025] and Martinet et al. [2022].

Because all models in Section 6.2.1 showed the best fit for the same combination of scale values and log-likelihoods steeply decreased for combinations showing larger V_{eff}, the tested scale value combinations were slightly adjusted, see Tab. 6.3. The relative quality of the fit is, again, indicated by the log-likelihood and can be seen in Fig. 6.5. The spiral arm models in both the OUV and the IR range show log-likelihoods that are far below the optimum, that is given by an double exponential model with scale values of $R_E = 5.0$ kpc, $h_E = 0.4$ kpc. These models are deemed as a rather bad fit for the Galaxy. Te qualities follow approximately the same trend as in Fig.6.3. The model maps combining exponential and gaussian features show the same log-likelihood here. Both spiral model present to

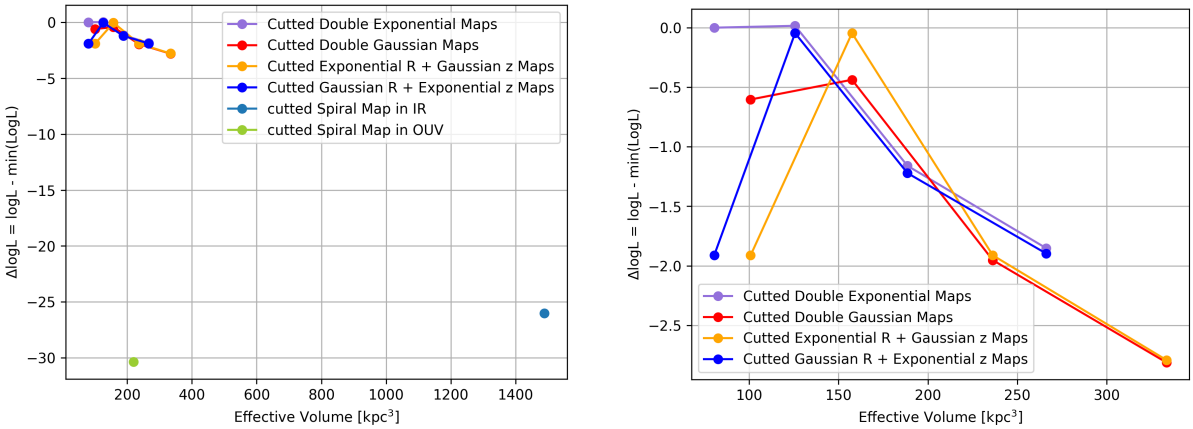

Figure 6.5: Both panels show the log-likelihood of cut models as a function of the effective volume. Because the spiral arm models result in log-likelihood values far below the best fit model, the right panel shows the plot without them. This large gap in log-likelihoods indicate that the spiral arm models provide a rather poor description of the spatial ^{26}Al distribution compared to the other models.

be relatively bad fits for the distribution of ^{26}Al. It is notable, that the second best fit was also achieved by a double exponential model (with $R_E = 4.0\,\mathrm{kpc}$, $h_E = 0.4\,\mathrm{kpc}$). In general the models tested with a combination of $R_E = 5.5\,\mathrm{kpc}$, $h_E = 0.7\,\mathrm{kpc}$ show to be rather bad for all models.

6.3 Flux and Mass values per Ring

The results of *spimodfit* yield the flux per ring for all models. As they are all quite similar only the results of the best fit for each model is shown in Fig. 6.6. Plots containing all fluxes per model and per combinations of scale values, can be found in the appendix A.2. In terms of flux models follow the same trend, and increase with the distance to the Galactic center. The analytic models show to be consistent to one another, leading to a very similar flux values throughout the Galaxy. The two spiral arm model, even though consistent in itself, continuously suggest more flux for the innermost 8 kpc than the other fits. All flux values are consistent within the 8-10 kpc ring. The biggest difference can be seen in the last ring, where all analytic models are consistent with zero, which is explained by the aged stellar population there, showing only low metallicity. Only the spiral models show a significant signal in this bin. These values do however have rather large uncertainties.

Eq. 5.8 and 5.9 can be used to calculate the mass per ring according to the values presented here. Because they depend on the reference flux F_{norm}, which is different for each sky

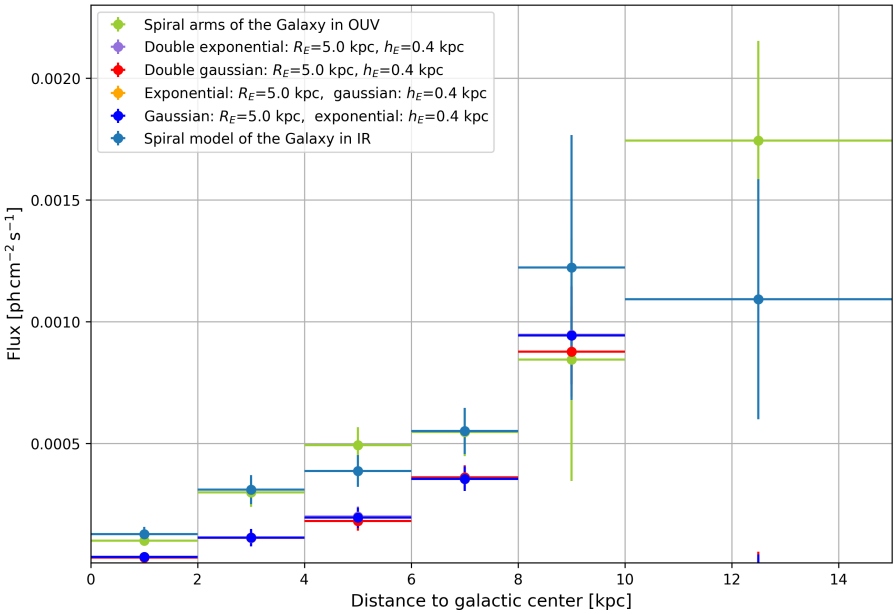

Figure 6.6: Flux results F_{fit} for the sky maps yielding the largest log-likelihood.

map, the masses for the same model with different scale values vary a lot more than the corresponding fluxes do.

The resulting mass for each analytic model can also be found in the appendix, while only the masses of the best fits can be seen in Fig. 6.7. They are compared to the prediction of the total model of Vasini et al. [2025] and we find a generally good agreement for the distribution. In the 8-10 kpc ring, the predictions of our measurement compared to the GCE model show the largest disagreement. This is explained by the probably somewhat enhanced ^{26}Al line flux in the local environment around the Sun due to numerous nearby young massive star regions [e.g., Diehl et al., 2010, Martin et al., 2012, Siegert and Diehl, 2017, Krause et al., 2018] and potentially from the Local Bubble [e.g., Schulreich et al., 2023, Siegert et al., 2024].

The same plot is shown for the results of non-rotating and rotating models of different initial masses from Martinet et al. [2022] in the lower panel. All models show barely any ^{26}Al budget beyond the 10 kpc ring, which is consistent with measurements. The non-rotating model of stars with initial masses up to 300 $M_\odot$ yields masses per bin, that stay way below our measurements and show generally bad agreement. The rotating model of the same masses shows better agreement but are still barely consistent with our model except for the 2-4 kpc bin where measurement and model slightly overlap in the 1σ confidence interval. The model considering rotating stars of 500 $M_\odot$ is in good agreement with measurements for the 2 kpc rings between 0-8 kpc. But shows a big gap in masses for 8-10 kpc. For non-rotating models of the same mass only rings between 2-6 kpc are consistent with measurements, while the bins first and fourth ring vary by a little more

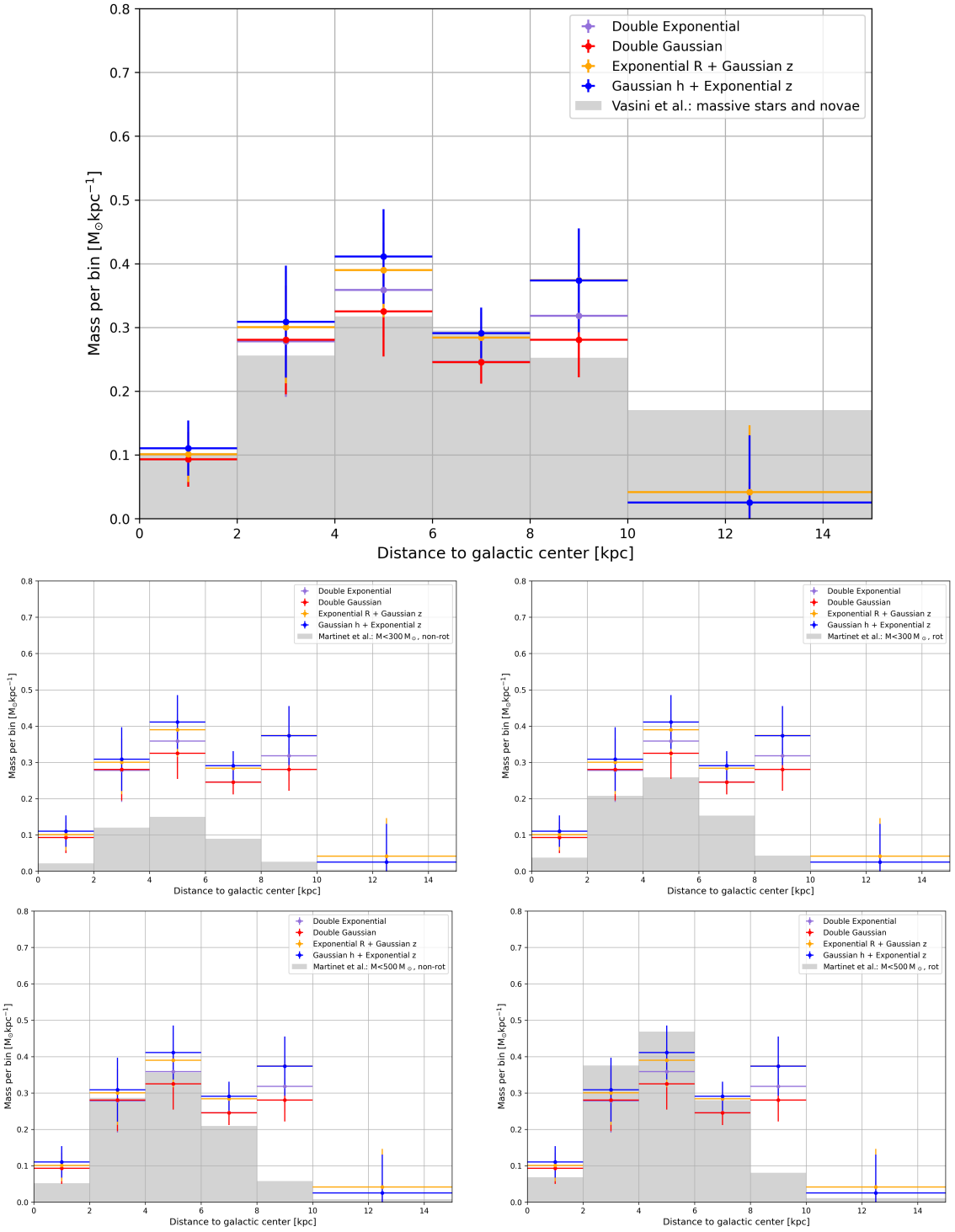

Figure 6.7: Resulting ^{26}Al masses per bin for the best fit per model compared to the mass predicted by Vasini et al. [2025] (*top*) and Martinet et al. [2022] (*bottom*).

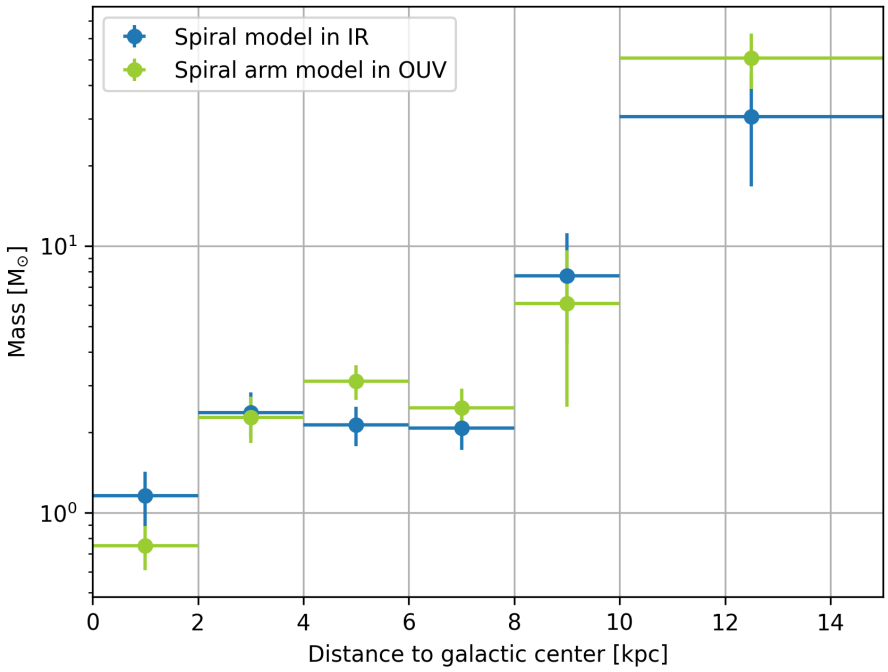

Figure 6.8: Masses suggested by spiral model bypass all other model predictions by far.

than 1σ.

In Fig. 6.8 the masses per ring resulting from the spiral models are given. Even though they are consistent within themselves, they predict a lot more ^{26}Al per ring than all other models. They also surpass previous estimates of the Galactic ^{26}Al mass by far. As they also have shown to be of rather bad fit towards the INTEGRAL/SPI dataset, this model proves to be insufficient in providing a quantitative estimate of the Galactic ^{26}Al budget and is probably not a good representation of the Galaxy as seen in the 1.8 MeV emission.

6.4 Contribution of classical novae and massive stars

The contribution of each source is determined by a χ^2 test (Eq. 4.9) The models predicting the mass of ^{26}Al as a function of Galactocentric distance were described in Section 5.1.2. Fig 6.9 shows the results as contour plots for the double exponential model. The color indicates intervals of significance in terms of sigma. We show the mass composition that is predicted by the model itself with an orange star and the parameters at χ^2 minimum with a pink dot. By calculating the distance of this dot to the edges of the first interval, the 1σ band is found. The dotted white line indicates parameter combinations that are equal to 1.0. If the values are normalized correctly, the best fit should always be found along this line. As discussed earlier, this normalization is done by considering the best

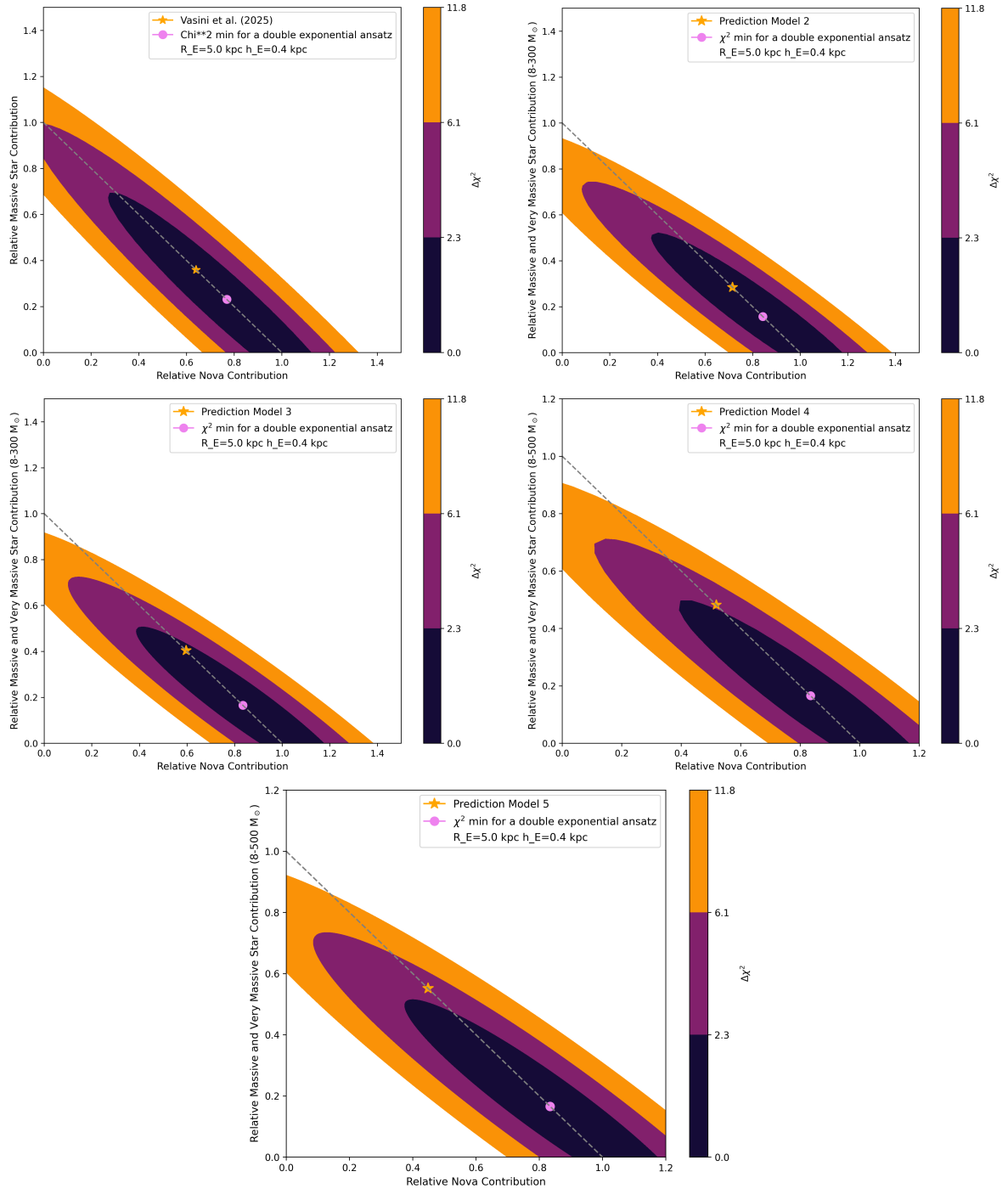

Figure 6.9: Results of the χ^2 test for an double exponential model. The yellow star marks the composition of ^{26}Al sources as predicted by the model. The pink dot the parameter combination for which χ^2 is minimal.

fit mass. Fig. 6.10 shows these best fit masses for three χ^2 fits. In indigo and purple, the distribution of the GCE is shown, while the measurements of SPI are indicated in black. The best fit mass combines ^{26}Al from all considered sources. Its distribution is given by Eq. 5.4 for the best parameter combination. The partial masses contributed by novae or (very) massive stars are also shown, together with the mass distribution that was measured with SPI. Fitting the mass model M towards the measured data we find a best fit for parameters a_{N} and a_{MS} and get a best fit Mass M_{bf}, according to Eq. 5.6. This is of course depending on the mass contribution, M_{N} and M_{MS}, considered in the distribution model. This best fit mass distribution can be seen in light blue in Fig. 6.10. Additionally, the best fit distribution of mass depending on the source is shown. These plots clearly illustrate how the best fit mass is shifted after fitting the GCE models. For the upper right panel, e.g., the best fit mass is pushed towards the bins between 2-8 kpc, when compared to the GCE predictions. While the model of Vasini et al. [2025] still predicts $\sim 0.1\,\mathrm{M}_{\odot}$ for the ring between 10-15 kpc, measurements are consistent with zero. At the same time predictions in the bins between 2-12 kpc are underestimating the measured values. The mass distribution must therefore be shifted towards these rings if they are fitted towards the measured data. This also shows, that barely any VMS contribution is needed to explain the distribution of the measurements. This can also be seen in the panel on the right: here the prediction for VMS is slightly shifted towards the center if compared to the prediction for novae. This leads to barely any VMS contribution as they cannot account for the ^{26}Al budget measured on the outer regions of the Galaxy.

We present the results of all tested models on the left side in Fig. 6.11 and find general good agreement between these values. All data points appearing between 40-60 % and at exactly 100 % of relative nova contribution are results of the spiral arm model and might therefore vary from the other data. On the right, we show the contour of the 1σ area.

All tested models predict a non-negligible contribution of ^{26}Al in the 1σ interval. While comparison to the Vasini et al. [2025] model can still predict up to 70 % of ^{26}Al originating from massive stars at the border of the 1σ confidence interval, all other models, i.e. models additionally considering VMS, predict less. In general, the confidence interval for Model 1 shows the steepest slope. That means, it includes more combinations in favor of higher massive star contribution than the other models. Models 2–5 are almost identical, even though the total mass per ring varies a lot. This is not surprising as the χ^2 only depends on the relative mass distribution which was very similar for all Martinet et al. [2022] predictions. All four models are consistent within the margin of the uncertainty. If we consider uncertainties within 2σ, only Model 1 allows to explain the distribution of Galactic ^{26}Al without the contribution of novae at the outer edge of the confidence interval. The other models predict at least 8 % of nova contribution at the border of the interval. The 2σ interval holds 95.4 % of normally distributed data, i.e. contributions

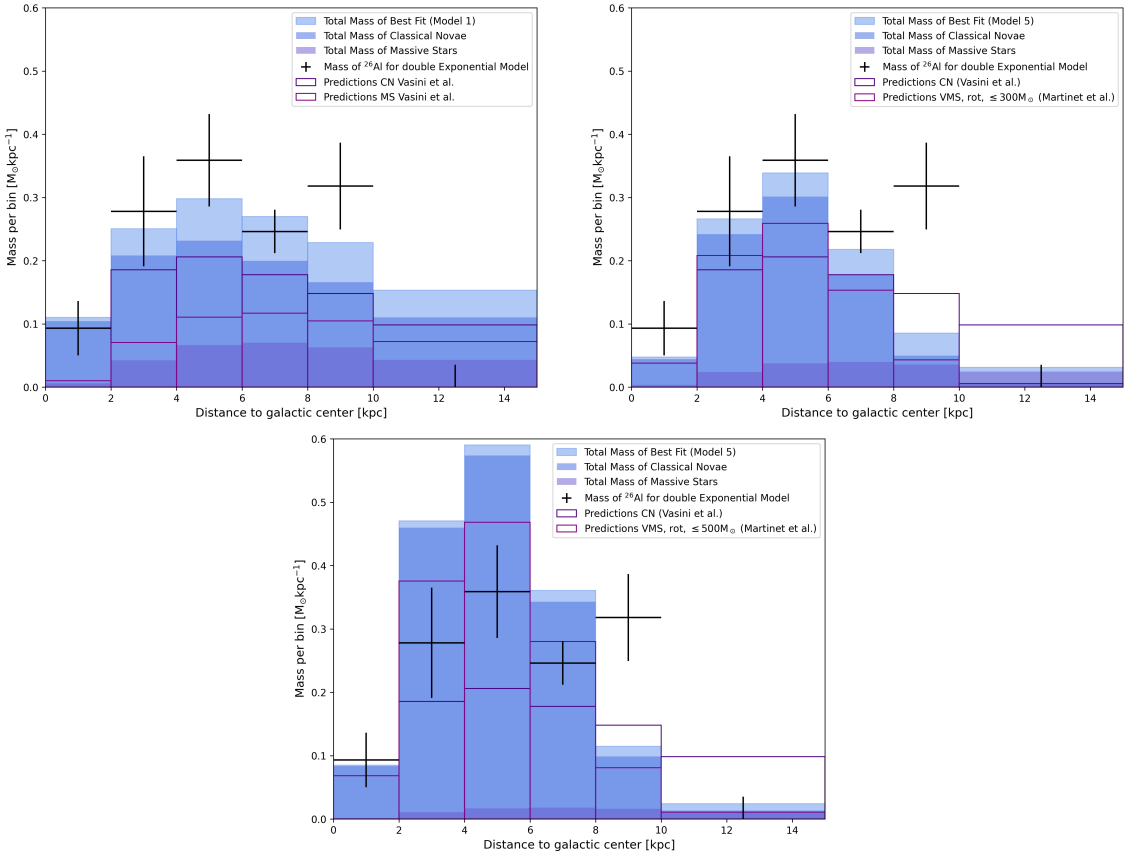

Figure 6.10: Here, results of INTEGRAL/SPI measurements are shown in black together with the GCE predictions, purple, for three exemplary fits. The total best fit mass, as well as the mass per source is given in shades of blue.

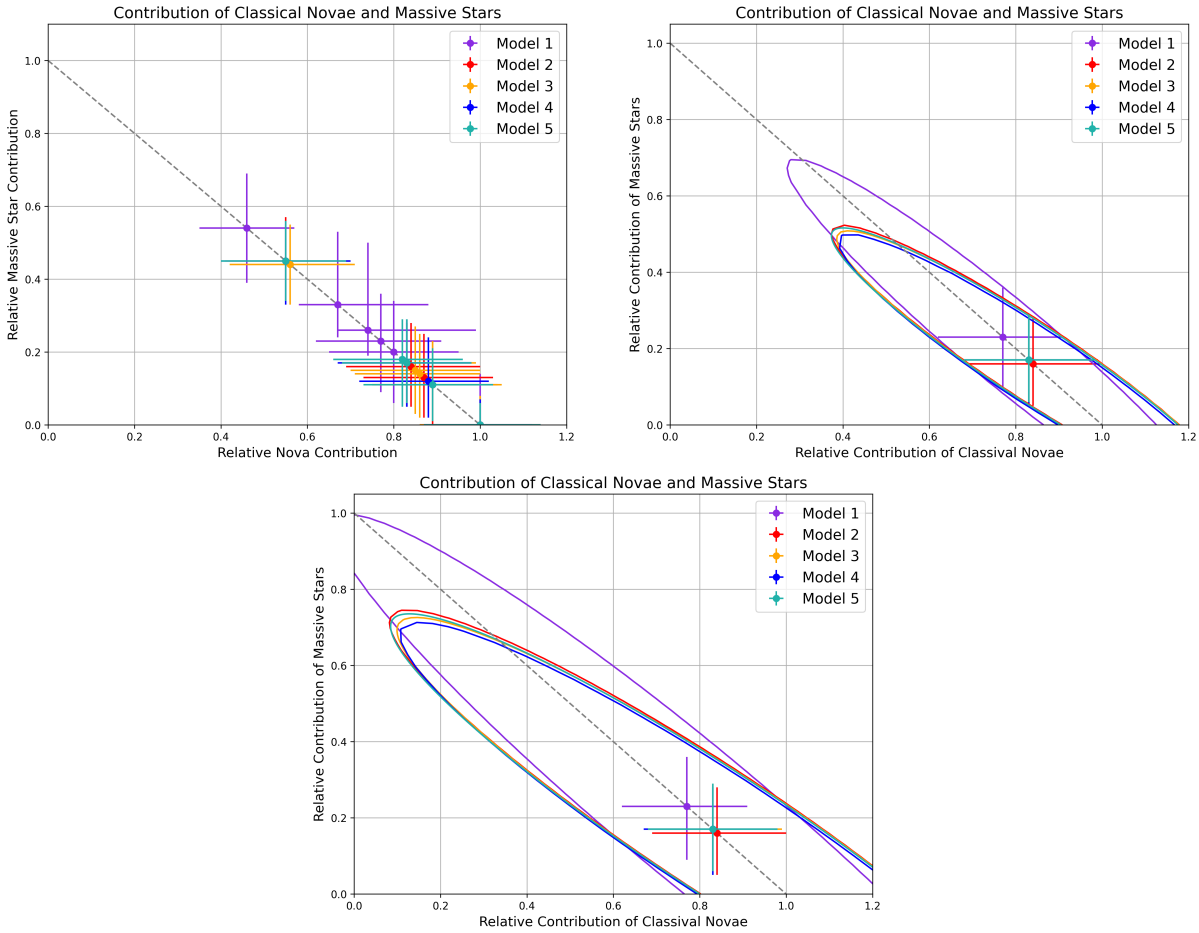

Figure 6.11: Results of the χ^2 tests for all combinations of models are shown on the upper left panel. On the upper right, the results of the best spatial model is shown including the 1σ confidence interval. All models show significant nova contribution to the Galactic budget. The 2σ interval is shown below. One of five models predict, that within 2σ confidence, the Galactic ^{26}Al can be explained by massive stars only. The other four show contributions of at least 8%.

	Contribution of Classical Novae	Contribution of Massive Stars
Model 1	$0.77^{+0.14}_{-0.15}$	$0.23^{+0.13}_{-0.14}$
Model 2	$0.84^{+0.16}_{-0.15}$	$0.16^{+0.12}_{-0.11}$
Model 3	$0.83^{+0.16}_{-0.15}$	$0.17^{+0.12}_{-0.12}$
Model 4	$0.83^{+0.15}_{-0.15}$	$0.17^{+0.11}_{-0.11}$
Model 5	$0.83^{+0.15}_{-0.15}$	$0.17^{+0.12}_{-0.11}$

Table 6.4: Relative contribution results of the two sources at χ^2 minimum for assuming a double exponential disk model. The uncertainties were calculated from the 1σ confidence intervals. In this case, at least 62% of Galactic ^{26}Al originates in novae.

beyond its border only appear in 4.6 % of cases and are more unlikely. This means, that the tested models predict a nova contribution of at least 62 % for minimal χ^2 parameter combinations. These might extend up to 91 %. The contribution predicted at minimum χ^2 for a double exponential disk are given in Tab. 6.4. These values exceed previous contribution estimates by far and are not in agreement with state of the art literature.

Chapter 7

Summary and Conclusion

In this theses, the hypothesis of possible novae contributions to Galactic ^{26}Al was investigated. This is motivated by ^{26}Al measurements inferring a SFR of $\gtrsim 5\,M_{\odot}\,\mathrm{yr}^{-1}$ [Siegert et al., 2023], which exceeds other estimates by up to a factor of four [e.g., Kennicutt and Evans, 2012, Licquia and Newman, 2015, Chomiuk and Povich, 2011].
Using line-of-sight integration, maps of the ^{26}Al emission for different spatial models are created and fit towards a 20 yr INTEGRAL/SPI dataset. By fitting six maps, representing concentric rings throughout the Galaxy, to the data, the mass distribution depending on the Galactocentric distance is determined. The quality of the fit is judged by their Log-likelihoods. A double exponential disk model shows the best results for a scale value combination of $z_E = 0.4\,\mathrm{kpc}$ and $R_E = 5.0\,\mathrm{kpc}$. To test a more physical model, the spiral arms as seen by their dust emission in the optical and ultraviolet as well as in the infrared energy range, described by Robitaille et al. [2012], are fit to the measurements as well. That resulted in log-likelihoods way above the best fit and masses that are not consistent with results from the other models. This is caused by the rather lose connection between the dust emission and ^{26}Al. While the dust density is highest in the center of the spiral arms, and stars are born in regions of high dust density, the stars need to evolve until they first emit ^{26}Al. At that point they have already moved outwards from the center of the spiral arms. The Galactic ^{26}Al is therefore shifted away from the spiral arms and is not traced well by the dust density [Kretschmer et al., 2013, Krause et al., 2015]. The spiral arms by Robitaille et al. [2012] are therefore ruled out as a good model for the Galactic ^{26}Al distribution.
The Galactic Chemical Evolution (GCE) model of Vasini et al. [2025] presents a theoretical prediction of the distribution of ^{26}Al depending on the source. They show how the ^{26}Al mass originating in massive stars peak comparably further away from the Galactic center than ^{26}Al originating in classical novae. All masses, except for the spiral arm models, are in good agreement with the predictions of Vasini et al. [2025]. Only the measurement bin between 8-10 kpc shows a somewhat enhanced mass, which is attributed to the numerous

amount of young stars in this regions as well as potential contributions of the Local Bubble. By assuming that the total mass is a linear combination of both source types, we find 77^{+14}_{-15} % nova and 23^{+13}_{-14} % massive star contributions for the GCE by Vasini et al. [2025]. This contains previous results of no negligible nova contributions in the outer 2σ band. As ^{26}Al might also be soured in very massive stars, they are also considered and the mass by novae distribution by Vasini et al. [2025] compared to the distribution of ^{26}Al by very massive stars [Martinet et al., 2022]. This however, results in an even higher relative nova contribution after fitting towards the data. The minimum nova contribution, that is needed in these models is ≥ 8 % in the two sigma or ≥ 37 % in the one sigma area.
To conclude this thesis, it can be said, that the contribution of classical novae ^{26}Al is much larger than previously estimated. All results indicate that the Galactic ^{26}Al distribution cannot be explained solely by massive stars and rather suggest that the majority is originating in classical novae. Of course, the tested models were rather simple smooth spatial models of the Galaxy as the tested spiral arm model proofed unfit to describe the sky as seen at 1.8 MeV. These smooth models might be biased towards certain solutions and it would be wise to try to find a better fitting model considering the spiral arms in these energy regimes. In further investigations the locally enhanced components also must be taken into account in the 1.8 MeV analysis, which might be explained by massive stars only. While this might weaken the conclusion, it is certainly not excluded that novae contribute significantly more than previously expected. Especially, after seeing how clearly they dominate the ^{26}Al production in this thesis. Of course, future measurements with improved gamma ray telescopes might also improve these results.
This might also motivate other theses and work. As of right now we have not achieved directly seen proof of the ongoing nucleosynthesis in novae. Similar to ^{26}Al, simulations predict ^{22}Na to be produced in nova explosions. While it gamma-ray line at 1.275 MeV has not been observed yet, it could be used as a tracer for nova explosions, as it's lifetime is long enough to sustain the opaque nova phase after the explosion. Studying ^{22}Na could improve the understanding of nova explosions and their distribution as it's gamma-rays can only be seen only from hours to months after the explosion. CRGO/COMPTEL and INTEGRAL/SPI searched for this emission, resulting in upper limits for the ^{22}Na mass. But future missions, like COSI, might be able to detect it in the future [Fougères et al., 2023].

Declaration of originality

I declare that I have authored this thesis independently, that I have not used other than the declared sources / resources, and that I have explicitly marked all material which has been quoted either literally or by content from the used sources.

Würzburg, September 18, 2025 Name Name M. Zimmermann

Acknowledgments

I would like to thank Thomas for the place in his group and the opportunity of this thesis. I've learned a lot of new things while working in his Group and I'm very grateful for my time there. I'm especially thankful for the chance to attend my first conference, even though I presented the nerve and courage of a very intimidated bunny shortly before my talk.
My thanks goes out to all members of AG Siegert for the nice time and lunch talks, that I really enjoyed.
I would also like to thank Daniel for his patience and reassurance when I needed it.

Appendix A

Additional plots

A.1 Flux per model

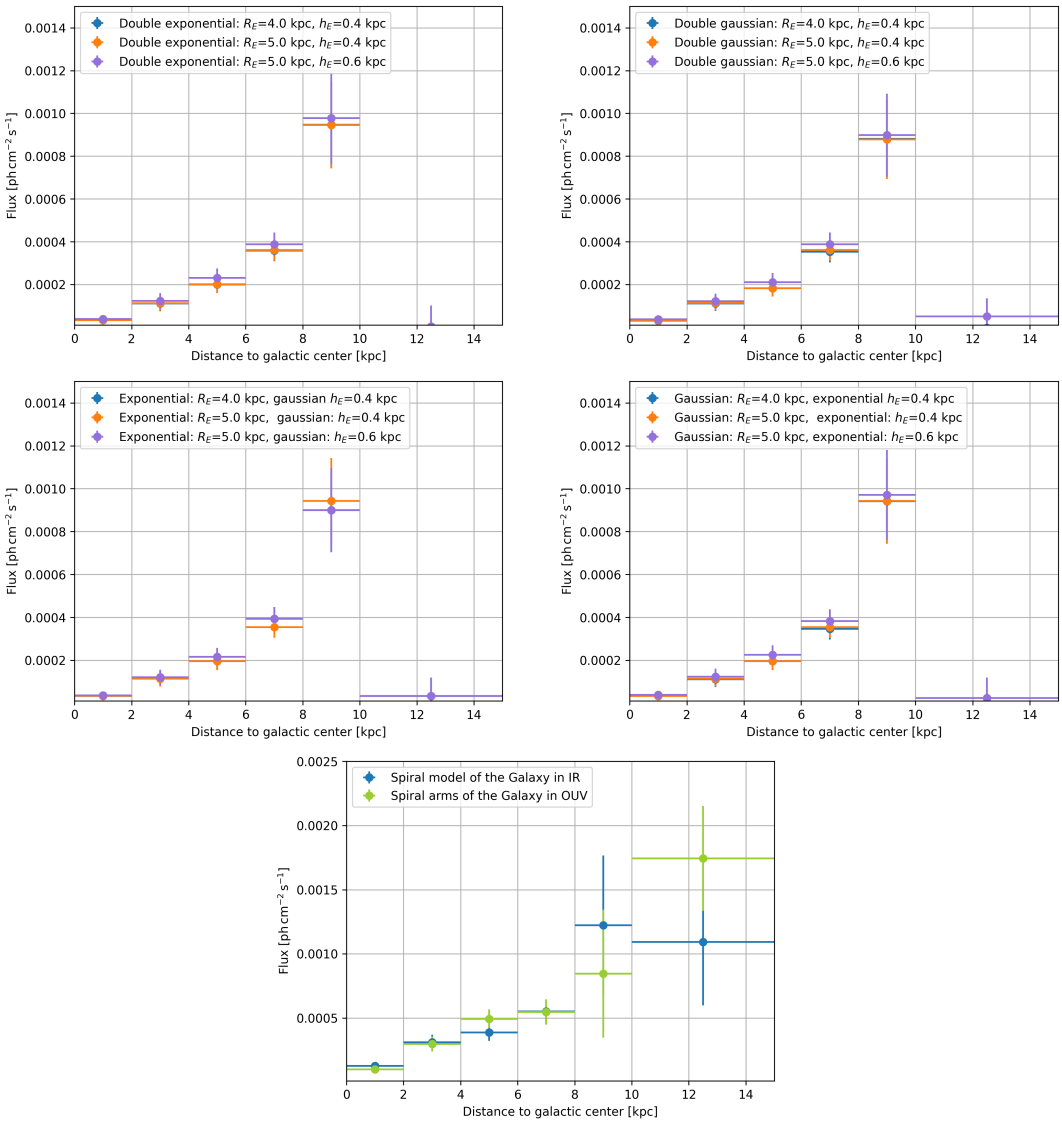

Figure A.1: Flux values per model and, for smooth models, tested scale value combination. All models show the best goodness-of-fit for the same combination of scale values $R_E = 5.0\,\text{kpc}$, $h_E = 0.4\,\text{kpc}$, marked in orange.

A.2 Mass per model

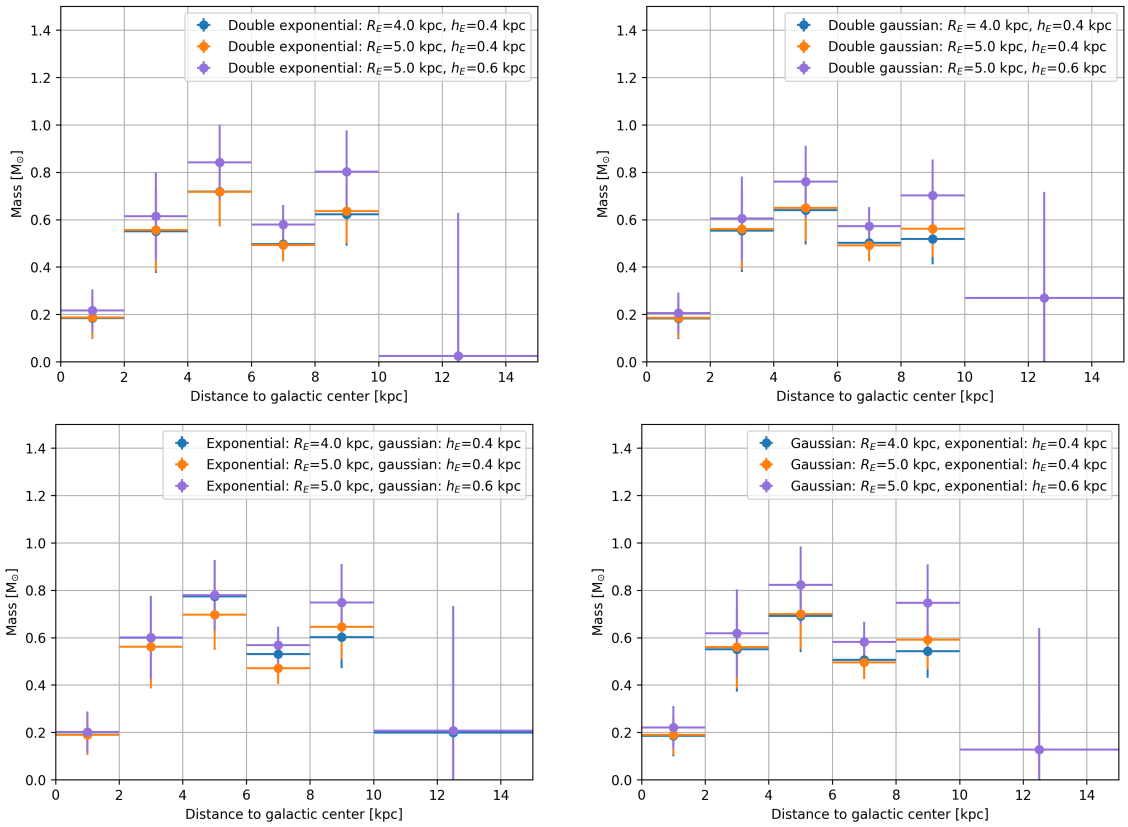

Figure A.2: Resulting masses of ^{26}Al per Galactic ring for six tested models with different scale value combinations.

Bibliography

H. Akaike. A New Look at the Statistical Model Identification. *IEEE Transactions on Automatic Control*, 19:716–723, January 1974.

W. D. Arnett. Gamma rays and supernova explosions. In C. E. Fichtel and F. W. Stecker, editors, *NASA Conference Publication*, volume 2 of *NASA Conference Publication*, pages 257–264, January 1977.

Björn Biltzinger, Jochen Greiner, J. Michael Burgess, and Thomas Siegert. Improving integral/spi data analysis of grbs. *Astronomy amp; Astrophysics*, 663:A102, July 2022. ISSN 1432-0746. doi: 10.1051/0004-6361/202243189. URL `http://dx.doi.org/10.1051/0004-6361/202243189`.

Laurent Bouchet, Elisabeth Jourdain, and Jean-Pierre Roques. The galactic 26al emission map as revealed by integral spi. *The Astrophysical Journal*, 801(2):142, mar 2015. doi: 10.1088/0004-637X/801/2/142. URL `https://dx.doi.org/10.1088/0004-637X/801/2/142`.

Jordi Casanova, Jordi José, and Steven N. Shore. Two-dimensional simulations of mixing in classical novae: The effect of white dwarf composition and mass. *Astronomy amp; Astrophysics*, 619:A121, November 2018. ISSN 1432-0746. doi: 10.1051/0004-6361/201833422. URL `http://dx.doi.org/10.1051/0004-6361/201833422`.

W. Cash. Parameter estimation in astronomy through application of the likelihood ratio. , 228:939–947, March 1979. doi: 10.1086/156922.

Laura Chomiuk and Matthew S. Povich. Toward a Unification of Star Formation Rate Determinations in the Milky Way and Other Galaxies. , 142(6):197, December 2011. doi: 10.1088/0004-6256/142/6/197.

T. J. L. Courvoisier, R. Walter, V. Beckmann, A. J. Dean, P. Dubath, R. Hudec, P. Kretschmar, S. Mereghetti, T. Montmerle, N. Mowlavi, S. Paltani, A. Preite Martinez, N. Produit, R. Staubert, A. W. Strong, J. P. Swings, N. J. Westergaard, N. White, C. Winkler, and A. A. Zdziarski. The INTEGRAL Science Data Centre (ISDC). , 411: L53–L57, November 2003. doi: 10.1051/0004-6361:20031172.

Wolfgang Demtröder. *Experimentalphysik 3 Atome, Moleküle und Festkörper*. Springer Spektrum, 2016. ISBN 978-3-662-49094-5.

R. Diehl, C. Dupraz, K. Bennett, H. Bloemen, W. Hermsen, J. Knoedlseder, G. Lichti, D. Morris, J. Ryan, V. Schoenfelder, H. Steinle, A. Strong, B. Swanenburg, M. Varendorff, and C. Winkler. COMPTEL observations of Galactic $\hat{2}6\hat{A}$l emission. , 298:445, June 1995.

R. Diehl, M. G. Lang, P. Martin, H. Ohlendorf, Th. Preibisch, R. Voss, P. Jean, J. P. Roques, P. von Ballmoos, and W. Wang. Radioactive ^{26}Al from the Scorpius-Centaurus association. , 522:A51, November 2010. doi: 10.1051/0004-6361/201014302.

Roland Diehl. Radioactive isotopes in the interstellar medium. *Astrophysics and Space Science*, 366:104, 2021. URL `https://doi.org/10.1007/s10509-021-04003-8`.

Roland Diehl, C. Dupraz, K. Bennett, H. Bloemen, J. Hermsen, W. Knödlsedler, G. Lichti, D. Morris, J. Ryan, V. Schönfelder, H. Steinle, A. Strong, B. Swanenburg, M. Varendorff, and C. Winkler. Comptel observations of galactic ^{26}al emission. *Astronomy and Astrophysics*, 298:445, 1994.

Roland Diehl, Hubert Halloin, Karsten Kretschmer, G. Lichti, V. Schönfelder, Andrew Strong, Andreas von Kienlin, Wei Wang, Pierre Jean, Jürgen Knödlseder, Jean-Pierre Roques, G. Weidenspointner, Stephane Schanne, Dieter Hartmann, Christoph Winkler, and Cornelia Wunderer. Radioactive al-26 from massive stars in the galaxy. *Nature*, 439:45–7, 02 2006. doi: 10.1038/nature04364.

Roland Diehl, Thomas Siegert, Jochen Greiner, Martin Krause, Karsten Kretschmer, Michael Lang, Moritz Pleintinger, Andrew W. Strong, Christoph Weinberger, and Xiaoling Zhang. INTEGRAL/SPI γ-ray line spectroscopy. Response and background characteristics. , 611:A12, March 2018. doi: 10.1051/0004-6361/201731815.

Roland Diehl, Martin G.H. Krause, Karsten Kretschmer, Michael Lang, Moritz M.M. Pleintinger, Thomas Siegert, Wei Wang, Laurent Bouchet, and Pierrick Martin. Steady-state nucleosynthesis throughout the galaxy. *New Astronomy Reviews*, 92, 2020.

C. Fougères, F. de Oliveira Santos, N. A. Smirnova, and C. Michelagnoli. Understanding the cosmic abundance of 22na: Lifetime measurements in 23mg. *EPJ Web of Conferences*, 279:09001, 2023. ISSN 2100-014X. doi: 10.1051/epjconf/202327909001. URL `http://dx.doi.org/10.1051/epjconf/202327909001`.

Arnold Hanslmeier. *Einführung in Astronomie und Astrophysik*. Springer Spektrum, 2020. ISBN 978-3-662-60413-7. URL `https://link.springer.com/book/10.1007/978-3-662-60413-7`.

Michael R. Hayden, Jon A. Holtzman, Jo Bovy, Steven R. Majewski, Jennifer A. Johnson, Carlos Allende Prieto, Timothy C. Beers, Katia Cunha, Peter M. Frinchaboy, Ana E. García Pérez, Léo Girardi, Fred R. Hearty, Young Sun Lee, David Nidever, Ricardo P. Schiavon, Katharine J. Schlesinger, Donald P. Schneider, Mathias Schultheis, Matthew Shetrone, Verne V. Smith, Gail Zasowski, Dmitry Bizyaev, Diane Feuillet, Sten Hasselquist, Karen Kinemuchi, Elena Malanushenko, Viktor Malanushenko, Robert O'Connell, Kaike Pan, and Keivan Stassun. Chemical Cartography with APOGEE: Large-scale Mean Metallicity Maps of the Milky Way Disk. , 147(5):116, May 2014. doi: 10.1088/0004-6256/147/5/116.

Matthias Heyssler. *Das Leben der Sterne, Teil II: Junge stellare Objekte und Sternenalltag*. Springer Spektrum, 2015. ISBN 978-3-658-09173-6. URL `https://link.springer.com/book/10.1007/978-3-658-09173-6`.

Matthias Heyssler. *Das Leben der Sterne, Teil III: Endphasen der Sterne*. Springer Spektrum, 2016. ISBN 978-3-658-10650-8. URL `https://link.springer.com/book/10.1007/978-3-658-10650-8`.

Jordi José and Margarita Hernanz. TOPICAL REVIEW: Nucleosynthesis in classical nova explosions. *Journal of Physics G Nuclear Physics*, 34(12):R431–R458, December 2007. doi: 10.1088/0954-3899/34/12/R01.

Jordi José. *STELLAR EXPLOSIONS: Hydrodynamics and Nucleosynthesis*. CRC Press, 2016. URL `http://www.fen.upc.edu/users/jjose/CRC-Downloads.html`.

Jordi José and Margarita Hernanz. Nucleosynthesis in classical novae: Co versus one white dwarfs. *The Astrophysical Journal*, 494(2):680, feb 1998. doi: 10.1086/305244. URL `https://dx.doi.org/10.1086/305244`.

Jordi José, Margarita Hernanz, and Christian Iliadis. Nucleosynthesis in classical novae. *Nuclear Physics A*, 777:550–578, 2006. ISSN 0375-9474. doi: https://doi.org/10.1016/j.nuclphysa.2005.02.121. URL `https://www.sciencedirect.com/science/article/pii/S0375947405002708`. Special Issue on Nuclear Astrophysics.

Robert C. Kennicutt and Neal J. Evans. Star formation in the milky way and nearby galaxies. *Annual Review of Astronomy and Astrophysics*, 50(Volume 50, 2012):531–608, 2012. ISSN 1545-4282. doi: https://doi.org/10.1146/annurev-astro-081811-125610. URL `https://www.annualreviews.org/content/journals/10.1146/annurev-astro-081811-125610`.

Chiaki Kobayashi, Hideyuki Umeda, Ken'ichi Nomoto, Nozomu Tominaga, and Takuya Ohkubo. Galactic Chemical Evolution: Carbon through Zinc. , 653(2):1145–1171, December 2006. doi: 10.1086/508914.

Martin G. H. Krause, Roland Diehl, Yiannis Bagetakos, Elias Brinks, Andreas Burkert, Ortwin Gerhard, Jochen Greiner, Karsten Kretschmer, and Thomas Siegert. ^{26}Al kinematics: superbubbles following the spiral arms?. Constraints from the statistics of star clusters and HI supershells. , 578:A113, June 2015. doi: 10.1051/0004-6361/201525847.

Martin G. H. Krause, Andreas Burkert, Roland Diehl, Katharina Fierlinger, Benjamin Gaczkowski, Daniel Kroell, Judith Ngoumou, Veronica Roccatagliata, Thomas Siegert, and Thomas Preibisch. Surround and Squash: the impact of superbubbles on the interstellar medium in Scorpius-Centaurus OB2. , 619:A120, November 2018. doi: 10.1051/0004-6361/201732416.

P. Kretschmar, C. Winkler, T. J.-L. Courvoisier, G. Di Cocco, R. Diehl, N. Gehrels, S. Grebenev, W. Hermsen, J. M. Mas-Hesse, F. Lebrun, and et al. The integral mission – an overview. *Proceedings of the International Astronomical Union*, 1(S230):59–65, 2005. doi: 10.1017/S1743921306007873.

Karsten Kretschmer, Roland Diehl, Martin Krause, Andreas Burkert, Katharina Fierlinger, Ortwin Gerhard, Jochen Greiner, and Wei Wang. Kinematics of massive star ejecta in the Milky Way as traced by ^{26}Al. , 559:A99, November 2013. doi: 10.1051/0004-6361/201322563.

M. Kubryk, N. Prantzos, and E. Athanassoula. Evolution of the Milky Way with radial motions of stars and gas. II. The evolution of abundance profiles from H to Ni. , 580: A127, August 2015. doi: 10.1051/0004-6361/201424599.

William R. Leo. *Techniques for nuclear and particle physics experiments*. Spriner Verlag Berlin Heidelberg, 1994.

Timothy C. Licquia and Jeffrey A. Newman. Improved estimates of the milky way's stellar mass and star formation rate from hierarchical bayesian meta-analysis. *The Astrophysical Journal*, 806(1):96, jun 2015. doi: 10.1088/0004-637X/806/1/96. URL `https://dx.doi.org/10.1088/0004-637X/806/1/96`.

W. A. Mahoney. Gamma-Ray Observations of Recently Synthesized Interstellar $_{26}$Al. In *Bulletin of the American Astronomical Society*, volume 16, page 879, September 1984.

P. Martin, A. W. Strong, P. Jean, A. Alexis, and R. Diehl. Galactic annihilation emission from nucleosynthesis positrons. , 543:A3, July 2012. doi: 10.1051/0004-6361/201118721.

Sébastien Martinet, Georges Meynet, Devesh Nandal, Sylvia Ekström, Cyril Georgy, Lionel Haemmerlé, Raphael Hirschi, Norhasliza Yusof, Matthieu Gounelle, and Vikram Dwarkadas. Very massive star winds as sources of the short-lived radioactive isotope 26al. *Astronomy amp; Astrophysics*, 664:A181, August 2022. ISSN 1432-0746. doi: 10.1051/0004-6361/202243474. URL http://dx.doi.org/10.1051/0004-6361/202243474.

National Nuclear Data Center (NNDC). Evaluated nuclear structure data file (ensdf), ^{25}mg. retrieved 17.9.2025.

U. Oberlack, K. Bennett, H. Bloemen, R. Diehl, C. Dupraz, W. Hermsen, J. Knoedlseder, D. Morris, V. Schoenfelder, A. Strong, and C. Winkler. The COMPTEL 1.809MeV all-sky image. , 120:311–314, December 1996.

Moritz M. M. Pleintinger, Siegert, Thomas, Diehl, Roland, Fujimoto, Yusuke, Greiner, Jochen, Krause, Martin G. H., and Krumholz, Mark R. Comparing simulated 26al maps to gamma-ray measurements. *AA*, 632:A73, 2019. doi: 10.1051/0004-6361/201935911. URL https://doi.org/10.1051/0004-6361/201935911.

S. Plueschke, R. Diehl, V. Schoenfelder, H. Bloemen, W. Hermsen, K. Bennett, C. Winkler, M. McConnell, J. Ryan, U. Oberlack, and J. Knoedlseder. The COMPTEL 1.809 MeV survey. In A. Gimenez, V. Reglero, and C. Winkler, editors, *Exploring the Gamma-Ray Universe*, volume 459 of *ESA Special Publication*, pages 55–58, September 2001. doi: 10.48550/arXiv.astro-ph/0104047.

N. Prantzos. An introduction to galactic chemical evolution. *EAS Publications Series*, 32:311–356, 2008. ISSN 1638-1963. doi: 10.1051/eas:0832009. URL http://dx.doi.org/10.1051/eas:0832009.

Nikos Prantzos and Roland Diehl. Radioactive ^{26}al in the galaxy: observations versus theory. *Physics Reports*, 267, 1996.

R. Ramaty and R. E. Lingenfelter. ^{26}Al: a galactic source of gamma-ray line emission. , 213:L5–L7, April 1977. doi: 10.1086/182397.

Thomas Robitaille, Ed Churchwell, Robert Benjamin, Barbara Whitney, Kenneth Wood, Brian Babler, and Marylin Meade. A self-consistent model of galactic stellar and dust infrared emission and the abundance of polycyclic aromatic hydrocarbons. *Astronomy and Astrophysics*, 545, 08 2012. doi: 10.1051/0004-6361/201219073.

Donatella Romano and Francesca Matteucci. Nova nucleosynthesis and Galactic evolution of the CNO isotopes. , 342(1):185–198, June 2003. doi: 10.1046/j.1365-8711.2003.06526.x.

H. Ruder, T. Ertl, F. Geyer, H. Herold, and U. Kraus. Line-of-sight integration: A powerful tool for visualization of three-dimensional scalar fields. *Computers Graphics*, 13(2): 223–228, 1989. ISSN 0097-8493. doi: https://doi.org/10.1016/0097-8493(89)90064-2. URL `https://www.sciencedirect.com/science/article/pii/0097849389900642`.

V. Schoenfelder, H. Aarts, K. Bennett, H. de Boer, J. Clear, W. Collmar, A. Connors, A. Deerenberg, R. Diehl, A. von Dordrecht, J. W. den Herder, W. Hermsen, M. Kippen, L. Kuiper, G. Lichti, J. Lockwood, J. Macri, M. McConnell, D. Morris, R. Much, J. Ryan, G. Simpson, M. Snelling, G. Stacy, H. Steinle, A. Strong, B. N. Swanenburg, B. Taylor, C. de Vries, and C. Winkler. Instrument Description and Performance of the Imaging Gamma-Ray Telescope COMPTEL aboard the Compton Gamma-Ray Observatory. , 86:657, June 1993. doi: 10.1086/191794.

M. M. Schulreich, J. Feige, and D. Breitschwerdt. Numerical studies on the link between radioisotopic signatures on Earth and the formation of the Local Bubble. II. Advanced modelling of interstellar ^{26}Al, ^{53}Mn, ^{60}Fe, and ^{244}Pu influxes as traces of past supernova activity in the solar neighbourhood. , 680:A39, December 2023. doi: 10.1051/0004-6361/202347532.

A. W. Shafter. The Galactic Nova Rate Revisited. , 834(2):196, January 2017. doi: 10.3847/1538-4357/834/2/196.

Steven N. Shore. Spectroscopy of novae – a user's manual, 2012. URL `https://arxiv.org/abs/1211.3176`.

Thomas Siegert and Roland Diehl. The ^{26}Al Gamma-ray Line from Massive-Star Regions. In Shigeru Kubono, Toshitaka Kajino, Shunji Nishimura, TadaAki Isobe, Shigehiro Nagataki, Tatsushi Shima, and Yoichi Takeda, editors, *14th International Symposium on Nuclei in the Cosmos (NIC2016)*, page 020305, January 2017. doi: 10.7566/JPSCP.14.020305.

Thomas Siegert, Roland Diehl, Christoph Weinberger, Moritz M. M. Pleintinger, Jochen Greiner, and Xiaoling Zhang. Background modelling for γ-ray spectroscopy with INTEGRAL/SPI. , 626:A73, June 2019. doi: 10.1051/0004-6361/201834920.

Thomas Siegert, Moritz M. M. Pleintinger, Roland Diehl, Martin G. H. Krause, Jochen Greiner, and Christoph Weinberger. Galactic population synthesis of radioactive nucleosynthesis ejecta. , 672:A54, April 2023. doi: 10.1051/0004-6361/202244457.

Thomas Siegert, Michael M. Schulreich, Niklas Bauer, Rudi Reinhardt, Saurabh Mittal, and Hiroki Yoneda. Gamma-ray line emission from the Local Bubble. , 689:A2, September 2024. doi: 10.1051/0004-6361/202450310.

A. W. Strong, R. Diehl, H. Halloin, V. Schönfelder, L. Bouchet, P. Mandrou, F. Lebrun, and R. Terrier. Gamma-ray continuum emission from the inner Galactic region as observed with INTEGRAL/SPI. , 444(2):495–503, December 2005. doi: 10.1051/0004-6361:20053798.

Tuguldur Sukhbold, T. Ertl, S. E. Woosley, Justin M. Brown, and H. T. Janka. Core-collapse Supernovae from 9 to 120 Solar Masses Based on Neutrino-powered Explosions. , 821(1):38, April 2016. doi: 10.3847/0004-637X/821/1/38.

F. X. Timmes, S. E. Woosley, D. H. Hartmann, R. D. Hoffman, T. A. Weaver, and F. Matteucci. 26al and 60fe from supernova explosions. *The Astrophysical Journal*, 449:204, August 1995. ISSN 1538-4357. doi: 10.1086/176046. URL `http://dx.doi.org/10.1086/176046`.

A. Vasini, E. Spitoni, F. Matteucci, G. Cescutti, and M. Della Valle. Tracing the Milky Way spiral arms with ^{26}Al: The role of nova systems in the 2D distribution of ^{26}Al. , 693:A37, January 2025. doi: 10.1051/0004-6361/202451630.

G. Vedrenne, J. P. Roques, V. Schönfelder, P. Mandrou, G. G. Lichti, A. von Kienlin, B. Cordier, S. Schanne, J. Knödlseder, G. Skinner, P. Jean, F. Sanchez, P. Caraveo, B. Teegarden, P. von Ballmoos, L. Bouchet, P. Paul, J. Matteson, S. Boggs, C. Wunderer, P. Leleux, G. Weidenspointner, Ph. Durouchoux, R. Diehl, A. Strong, M. Cassé, M. A. Clair, and Y. André. SPI: The spectrometer aboard INTEGRAL. , 411:L63–L70, November 2003. doi: 10.1051/0004-6361:20031482.

S. S. Wilks. The Large-Sample Distribution of the Likelihood Ratio for Testing Composite Hypotheses. *Annals Math. Statist.*, 9(1):60–62, 1938. doi: 10.1214/aoms/1177732360.

S. E. Woosley and Thomas A. Weaver. The Evolution and Explosion of Massive Stars. II. Explosive Hydrodynamics and Nucleosynthesis. , 101:181, November 1995. doi: 10.1086/192237.